

1
2
3
4
5
6
7
8
9
10
11
12
13
14
15
16
17
18
19
20
21
22

Archaeomagnetism in the Levant and Mesopotamia reveals the largest changes in the geomagnetic field

Ron Shaar¹, Yves Gallet², Yoav Vaknin^{1,3}, Lilach Gonen¹, Mario A. S. Martin³, Matthew J. Adams⁴, Israel Finkelstein^{3,5}

¹ The Institute of Earth Sciences, The Hebrew University of Jerusalem, Jerusalem, 91904, Israel

² Université Paris Cité, Institut de Physique du Globe de Paris, CNRS, 75005, Paris, France

³ Institute of Archaeology of Tel Aviv University, Tel Aviv 6997801, Israel

⁴ W.F. Albright Institute of Archaeological Research, Jerusalem, Israel

⁵ School of Archaeology and Maritime Cultures, University of Haifa, Haifa, Israel

Corresponding author: Ron Shaar (ron.shaar@mail.huji.ac.il)

Key Points:

- Archaeomagnetic intensity data from 23 groups of pottery collected from 18 consecutive radiocarbon-dated strata in Tel Megiddo (Israel).
- The Levantine Archaeomagnetic Curve (LAC): a Bayesian radiocarbon-calibrated archaeointensity curve of the Levant and Mesopotamia.
- Four geomagnetic spikes between 1050–600 BCE define new constraints for maximum field intensity and secular variation rates.

23 **Abstract**

24 Our understanding of geomagnetic field intensity prior to the era of direct instrumental
25 measurements relies on paleointensity analysis of rocks and archaeological materials that serve
26 as magnetic recorders. Only in rare cases absolute paleointensity datasets are continuous over
27 millennial timescales, in sub-centennial resolution, and directly dated using radiocarbon. As a
28 result, fundamental properties of the geomagnetic field, such as its maximal intensity and change
29 rate have remained a subject of lively discussion. Here, we place firm constraints on these two
30 quantities using Bayesian modeling of well-dated archaeomagnetic intensity data from the
31 Levant and Upper Mesopotamia. We report new data from 23 groups of pottery collected from
32 18 consecutive radiocarbon-dated archaeological strata from Tel Megiddo, Israel. In the Near
33 East, the period of 1700–550 BCE is represented by 84 groups of archaeological artifacts, 55 of
34 which were dated using radiocarbon or a direct link to clear historically-dated events, providing
35 unprecedented sub-century resolution. Moreover, stratigraphic relationships between samples
36 collected from multi-layered sites enable further refinement of the data ages. The Bayesian curve
37 shows four geomagnetic spikes between 1050 and 600 BCE, with virtual axial dipole moment
38 (VADM) reaching values of 155–162 ZAm^2 – much higher than any prediction from
39 geomagnetic field models. Rates of change associated with the four spikes are ~ 0.35 – 0.55
40 $\mu T/year$ (~ 0.7 – $1.1 ZAm^2/year$), at least twice the maximum rate inferred from direct observations
41 spanning the past 190 years. The increase from 1750 BCE to 1030 BCE (73 to 161 ZAm^2)
42 depicts the Holocene's largest change in field intensity.

43

44 **Plain Language Summary**

45 The strength of Earth's magnetic field is changing in an unpredictable manner. Understanding
46 these changes requires precise information on how the field has changed in the past. Direct
47 instrumental measurements of magnetic field intensity began in the 1840s, providing only a short
48 time window into past intensity changes. Here, we explore the more ancient field by analyzing a
49 rare collection of radiocarbon-dated archaeological materials from stratified archaeological
50 settlements and historically-dated burnt structures in the Levant and Mesopotamia. We use new
51 data from Tel Megiddo (Armageddon) to construct a continuous curve of geomagnetic field
52 intensity spanning 2500 years, with unprecedented detail and resolution. The curve depicts the
53 evolution of a high-intensity anomaly, the largest change in intensity observed during the
54 Holocene. Between 1750 and 1050 BCE, the field rapidly increased to values greater than twice
55 those of today, much higher than any prediction derived from available geomagnetic field
56 models. Subsequent oscillations between 1050 and 550 BCE, with extreme peaks, namely
57 'geomagnetic spikes', reveal change rates of at least twice as fast as the fastest change observed
58 since the advent of direct measurements. Levantine archaeomagnetic data represent a case study
59 in which archaeology provides crucial constraints on the geomagnetic field behavior.

60 **1. Introduction**

61 The absolute intensity of the geomagnetic field was first measured by Carl Friedrich Gauss in
62 1832 (Courtillet & Le Mouel, 2007). Subsequent measurements with improved precision and
63 spatial resolution have provided quantitative estimates of the amplitude and rate of geomagnetic
64 field intensity changes, but only across the past two centuries. Information from periods
65 preceding observational measurements, fundamental for understanding the magnetic field

66 behavior, is derived from ancient materials that acquired thermoremanent magnetization upon
67 cooling from high temperatures. For the past several millennia, archaeological materials have
68 been the primary source for this information (e.g., Arneitz et al., 2017; Brown et al., 2021),
69 providing most of the data for late Holocene geomagnetic models (Arneitz et al., 2019;
70 Campuzano et al., 2019; Constable et al., 2016; Nilsson et al., 2014; Nilsson et al., 2022;
71 Panovska et al., 2019; Pavon-Carrasco et al., 2014). However, global models are smoothed by
72 design, as they require a tradeoff between model complexity and fit to heterogeneous data.
73 Regional intensity curves provide important insights into field behavior (e.g., Cai et al., 2017;
74 Garcia et al., 2021; Genevey et al., 2016, 2021; Rivero-Montero et al., 2021; Schnepf et al.,
75 2020), but they depend on the quality of the underlying source data. One of the most significant
76 limiting factors for both global and regional field modeling is the limited precision and accuracy
77 of the published ages. Only ~12% of the global published data from the past 10ky data are
78 directly dated with radiocarbon, and in many cases, the exact nature and context of the dated
79 material are not documented. Instead, most archaeomagnetic ages are based on assignment to
80 regional archaeological chronologies, which may have differing interpretations, can be poorly
81 tied to absolute ages, or have large age ranges (e.g., Shaar et al., 2020). Furthermore, unlike
82 paleomagnetic field direction reconstructions, which use stratigraphic constraints in sedimentary
83 sequences to obtain continuous time series, archaeomagnetic intensity datasets are mostly
84 sporadic in time and space. Given the overall uncertainties in the available paleomagnetic and
85 archaeomagnetic data, some of the most fundamental properties of the geomagnetic field, such as
86 its maximum intensity and maximum possible change rate, have remained elusive and the subject
87 of a lively and fruitful debate (Davies & Constable, 2018; Korte & Constable, 2018; Livermore
88 et al., 2014; Livermore et al., 2021).

89 One way to improve the resolution of archaeomagnetic data is to focus efforts on large multi-
90 layered archaeological sites, which are composed of distinct consecutive strata, and can provide
91 data in stratigraphic order, e.g., Mari (Tell Hariri), Tell Atij and Tell Gudeda in Upper
92 Mesopotamia (Gallet & Butterlin, 2015; Gallet et al., 2020; Gallet et al., 2006; Gallet et al.,
93 2008), Ebla (Tell Mardikh) in Northern Levant (Gallet et al., 2014; Gallet et al., 2008), and Tel
94 Hazor in Southern Levant (Shaar et al., 2020; Shaar et al., 2016). Although these are key sites for
95 Near Eastern archaeology, most of their archaeomagnetic data are not radiocarbon-dated. From
96 this perspective, Tel Megiddo (Israel), with a radiocarbon-based age model covering timespan of
97 3000-735 BCE time-span, is unique, providing an unprecedented opportunity to construct a
98 stratigraphically constrained radiocarbon-calibrated archaeomagnetic time series.

99 In the following, we report the data obtained from Tel Megiddo, which to date, is the largest
100 archaeomagnetic intensity dataset available from a single site. We compile the new data with
101 other archaeomagnetic data from the Levant and Mesopotamia that pass our selection criteria.
102 The temporal resolution of the combined data between the 18th and the 6th century BCE is a
103 century or less, as most of the archaeomagnetic ages in this period are derived from radiocarbon-
104 dated contexts and historically-dated burnt structures. Using this high-precision compilation, we
105 develop the Levantine Archaeomagnetic intensity Curve (LAC), utilizing a Bayesian
106 methodology. The LAC elucidates the details of the largest geomagnetic change in the Holocene,
107 associated with the Levantine Iron Age Anomaly (Shaar et al., 2016) and the occurrence of
108 geomagnetic spikes (Ben-Yosef et al., 2009; Shaar et al., 2011; Shaar et al., 2016). We use the
109 LAC to enhance knowledge of the number, duration, and intensity of geomagnetic spikes, which
110 define new robust upper limit constraints for both maximum field intensity and change rate.

111 2. Archaeomagnetic intensity stratigraphy of Tel Megiddo

112 2.1. Background

113 Tel Megiddo (32.585N, 35.185E, Fig. 1) is a world-heritage archaeological site located on the
114 western margins of the Jezreel Valley in northern Israel. Owing to its strategic location on the
115 international route which connected Egypt with Mesopotamia, Megiddo was a central city and an
116 important administrative center throughout the Bronze and Iron Ages (ca. 3500 – 600 BCE).
117 Extensive excavations of the mound have revealed more than thirty Bronze and Iron Age
118 superimposed settlements, with several destruction layers indicating violent endings in military
119 campaigns (Finkelstein, 2009). The chronology of the entire Megiddo sequence was established
120 from Bayesian analyses of ca. 150 radiocarbon samples (the total number of radiocarbon samples
121 at Megiddo is 185) carefully collected from nearly all strata (Boaretto, 2022; Martin et al., 2020;
122 Regev et al., 2014; Toffolo et al., 2014). Special care was taken in assembling the radiocarbon
123 model from mostly short-lived organic materials strongly linked to the archaeological findings.
124 The exceptionally large radiocarbon data from a detailed, continuous, and well-established
125 stratigraphy, along with the intensive ceramic record of Megiddo that defines the relative dating
126 of the region (e.g., late Iron I, early Iron IIA), provides a robust absolute chronology for Near
127 Eastern archaeology.

128 The archaeomagnetic stratigraphy of Tel Megiddo is based on twenty-three different contexts
129 recovered from 18 layers, excavated in six excavation areas (Fig. 2). Ten contexts (S-3, H-15, K-
130 6, H-11, K-4/H-9/Q-7, Q-4, H-3/Q-2) are destruction layers with distinct boundaries and clear
131 marks of their ending. Megiddo's final destruction by the Assyrian Tiglath-Pileser III is
132 conclusively dated to 732 BCE, based on multiple historical documents. We sampled fragments
133 of indicative pottery from each context, with emphasis on local domestic material. We preferred,
134 when possible, complete or cured vessels that were photographed and documented in the
135 excavation reports. In three contexts (Q-4, Q-5, K-9), we also sampled fragments of cooking
136 ovens (tabuns). The fragments (termed hereafter ‘samples’ for consistency with previous
137 publications) discussed here include new data, as well as data already published in Shaar et al.
138 (2016) and Shaar et al. (2020), which reported the initial archaeomagnetic stratigraphy of
139 Megiddo. Supplementary Table S1 lists the archaeological details of all the materials analyzed in
140 this study.

141 2.2. Archaeointensity experiments

142 Thellier-IZZI-MagIC paleointensity experiments were conducted in the shielded paleomagnetic
143 laboratory at the Institute of Earth Sciences, the Hebrew University of Jerusalem, using two
144 modified ASC TD-48 ovens and a 2G-RAPID superconducting rock magnetometer (SRM).
145 Specimens were prepared by gluing small pieces of pottery inside non-magnetic $22 \times 22 \times 20$
146 mm square alumina crucibles. The protocol followed the IZZI method (Tauxe & Staudigel, 2004;
147 Yu et al., 2004) with routine pTRM checks at every second temperature step using an oven field
148 of 40, 50, or 60 μT . Heating time ranged from 40 to 65 minutes, depending on the target
149 temperature. In total, each IZZI experiment included 31 or 33 heating steps at 13 or 14
150 temperature intervals between 100°C to 590°C or 600°C. All specimens were subjected to
151 anisotropy of thermoremanent magnetization (ATRM) experiments, which consisted of eight
152 heating steps at 590°C or 600°C: a baseline zero-field step, six infield steps at orthogonal

153 directions, and an additional alteration check. ATRM alteration parameter was calculated
154 following Shaar et al. (2015) (Table 1). For specimens with ATRM alteration checks > 6%,
155 anisotropy of anhysteretic remanent magnetization (AARM) was measured at a 100mT AC field
156 in 0.1mT DC bias field, at six orthogonal directions, after thermal demagnetization of the
157 specimens. All specimens were subjected to cooling rate correction experiments, which consisted
158 of 4–5 cooling steps from 590 °C or 600 °C to room temperature, following the protocol
159 described in Shaar et al. (2020). Archaeointensity values were calculated with the *Thellier-GUI*
160 program (Shaar & Tauxe, 2013), incorporated into the *PmagPy* software package (Tauxe et al.,
161 2016), using *Thellier Auto Interpreter* algorithm and the acceptance criteria listed in Table 1.
162 Sample results were calculated by averaging at least 3 specimens per sample using the STDEV-
163 OPT algorithm of the *Thellier-GUI* program and the ‘extended error bounds’ approach (Shaar &
164 Tauxe, 2013; Shaar et al., 2016). When averaging sample data in ‘groups’ (see section 2.3), we
165 calculated a simple mean of the STDEV-OPT values of the samples. A detailed description of
166 the methods can be found in Shaar et al. (2016) and Shaar et al. (2020). All measurement data
167 are available in the MagIC database (earthref.org/MagIC/19395).

168

169 2.3. Results

170 The archaeomagnetic data from Tel Megiddo, including the data already published in Shaar et al.
171 (2016) and Shaar et al. (2020), include 763 specimens from 175 samples. In this study, we
172 analyze 288 specimens from 85 newly collected samples. In total, 583 specimens and 132
173 samples pass the criteria listed in Table 1, where archaeointensities obtained at the sample level
174 are calculated from a minimum of 3 specimens. Fig. 3 shows representative cases of a successful
175 specimen and interpretations failing criteria. The importance of the anisotropy and cooling rate
176 corrections is illustrated in Fig. 4. Typically, the bias due to anisotropy and cooling rate effects is
177 5%–15%; in some cases, the combined corrections exceed 20%. Table S2 (Supplementary
178 Material) lists specimens results, anisotropy and cooling rate correction factors, and values of
179 paleointensity statistics listed in Table 1.

180 Fig. 5 displays sample data with error bars calculated using the “extended error bounds”
181 approach (Shaar & Tauxe, 2013). In general, samples collected from the same archaeological
182 context (termed hereafter ‘group’) show good agreement with only two outliers in groups K-4
183 and Q-4. Levels H-9 and H-3 exhibit a large dispersion of data, with distinctively different
184 values. As the ceramics in each context represent production during a time interval rather than a
185 singular point in time, this probably indicates fast changes in the field during the interval
186 represented in the ceramic assemblage. Thus, we tentatively split the results from these two
187 contexts into two subgroups. The mean archaeointensity of each group is calculated by averaging
188 the sample means. Detailed sample data are provided in Table 2 and Supplementary Table S3.
189 The archaeomagnetic stratigraphy presented in Fig. 5 (Table 2) shows exceptionally large
190 amplitude changes – between ~39 and ~90 μ T. In the following sections, we explore in detail
191 this amplitude change depicted in the Megiddo data.

192 The ages of the groups are based on the Bayesian age model of Megiddo, which is assembled
193 from ~150 radiocarbon samples and takes into account the stratigraphic relationships between
194 strata and correlation between levels excavated at different areas (e.g. Fig. 2a). The published
195 68.2% and 95.4 % probability age intervals (Boaretto, 2022; Martin et al., 2020; Regev et al.,

196 2014; Toffolo et al., 2014) are shown in Table 2. The actual age ranges we use for the
 197 archaeomagnetic analysis overlap the radiocarbon age ranges, but are not identical. This
 198 distinction is performed to optimally represent the age range of the ceramic assemblage in each
 199 archaeological context, considering the entire archaeological and historical evidence. Thus, the
 200 age range of a group may be as short as 50 years for sequences of short-lived phases punctuated
 201 by well-dated destruction layers (e.g. Q-4,Q-5,Q-6,Q-7) or 250–300 years for less-constrained
 202 strata (e.g. J-4,J-5,J-6).

203 **3. The Levantine Archaeomagnetic Curve (LAC.v.1.0)**

204 The Levantine Archaeomagnetic Curve (LAC) is designed to enable both the statistical analysis
 205 of secular variation properties and archaeomagnetic dating. In this article, we focus on the
 206 geomagnetic implications of the curve, whereas in a sister article (Vaknin et al., in press), we
 207 demonstrate the applications of the curve for correlating ancient historical events. Preliminary
 208 versions of the LAC, using an identical methodology as in this study but spanning different time
 209 intervals, were published in Shaar et al. (2020) and Gallet et al. (2020). Here, we provide a short
 210 description of the different datasets used to construct the LAC and briefly outline the underlying
 211 methodology of the Bayesian analysis. A more detailed description of the archaeomagnetic
 212 methods, selection criteria, and our approach for sorting and organizing the published data can be
 213 found in Shaar et al. (2020). A complete description of the Bayesian method is given in
 214 Livermore et al. (2018).

215 **3.1. Data compilation: experimental guidelines**

216 Archaeomagnetic studies in the Levant and Mesopotamia, in the area extending from Egypt in
 217 the south to southern Turkey in the north, yielded an incredibly large archaeomagnetic dataset,
 218 which includes more than 722 archaeointensity estimates published between 1969 and 2021 and
 219 available in the GEOMAGIA50 database (Brown et al., 2015; Brown et al., 2021), the MagIC
 220 database (Tauxe et al., 2016), and the ArcheoInt compilation (Genevey et al., 2008). Yet, when
 221 these data are simply stacked together, significant discrepancies are evident (Supplementary
 222 Material, Fig. S1). From an experimental perspective, screening out the most robust data and
 223 assigning a consistent archaeointensity uncertainty to the overall data are not trivial tasks due to
 224 large differences in laboratory methods, data analysis approaches, and selection criteria.
 225 Moreover, not all of these data were published along with the raw measurement data, preventing
 226 a rigorous and identical calculation of the experimental uncertainty. We, therefore, adopt an
 227 approach that utilizes only methods that were tested against each other in different laboratories
 228 and shown to yield statistically indistinguishable results at the sample level:

- 229 • Thellier-IZZI-MagIC: This method incorporates the Thellier-IZZI protocol (Yu et al., 2004)
 230 exactly as applied in this study. The automatic interpretation procedure follows the STDEV-
 231 OPT algorithm (Shaar & Tauxe, 2013) with the ‘LAC criteria’ provided in Table 1. All
 232 measurement data are available in the MagIC database (<https://www.earthref.org/MagIC>) and
 233 can be re-interpreted using any set of alternative selection criteria.
- 234 • Triaxe (Le Goff & Gallet, 2004) or the Triaxe + Coe (Gallet & Le Goff, 2006): The Triaxe
 235 method was tested against the Thellier-IZZI-MagIC in a blind test in Shaar et al. (2020) and
 236 yielded indistinguishable results. The Triaxe + Coe includes groups of specimens, which

237 were analyzed using both the Thellier-Coe method (Coe et al., 1978) by Genevey et al.
238 (2003) and the Triaxe method by Gallet and Le Goff (2006), and found to be equivalent.

239 Other data will be included in future LAC compilations if the measurement data can be analyzed
240 using identical procedures and selection criteria as the rest of the LAC data.

241 Another aspect of the LAC compilation is associated with data hierarchy. A portion of the
242 published archaeomagnetic data was reported as averages of specimens prepared from the same
243 mother sample, while another portion was reported as averages of specimens or samples
244 collected from the same archaeological context. In the LAC compilation, we use the latter
245 approach to avoid over (under)-representation of contexts with more (fewer) samples and to
246 ensure that uncertainties are calculated consistently. Thus, each datum in the LAC compilation
247 represents a 'group', where a group can be, for example, a collection of indicative pottery from a
248 specific stratum, fired mud bricks from a burnt structure, a layer in a slag mound, or storage jars
249 with identical stamp types. The archaeointensity value of a group is calculated as a simple
250 average of the samples' means after screening out outliers (e.g., K-4 and Q-4 in figure 5). Two
251 exceptions to this rule are related to destruction layers: a kiln from Horvat Tevet that had gone
252 out of use when the site had been destroyed (Vaknin et al., in press) and a clay-made floor burnt
253 during the historically-dated Babylonian destruction (Vaknin et al., 2020); in these cases, a large
254 number of specimens collected from the same thermal unit are averaged.

255 Fig. 6 displays 142 groups between 3000 – 500 BCE passing the experimental criteria. In order
256 to minimize effects related to spatial variability of the field, we constrain the geographic
257 distribution of the data to the region that extends between southern Israel, Cyprus, northern
258 Syria, and eastern Syria (Fig. 1), comprising a circle with a radius of ~500km. Data are displayed
259 in terms of virtual axial dipole moment (VADM) – a transformation from local, latitude-
260 dependent field intensity measurement to the equivalent geomagnetic axial dipole moment. Data
261 from Syria (analyzed using the Triaxe or Triaxe+Coe methods) representing Mesopotamia and
262 northern Levant (Gallet & Al-Maqdissi, 2010; Gallet & Butterlin, 2015; Gallet et al., 2014;
263 Gallet et al., 2020; Gallet et al., 2006; Gallet et al., 2008; Genevey et al., 2003; Livermore et al.,
264 2021), were reported as groups and displayed as published with few minor updates on the ages of
265 some fragment groups (Supplementary Text S4 and the mentioned references for all the data
266 obtained at the specimen/fragment levels). Data from Timna-30 slag mound (Shaar et al., 2011),
267 Tel Hazor (Shaar et al., 2016), and the Judean stamped jars (Ben-Yosef et al., 2017), which were
268 published as samples, are averaged to represent group means (Supplementary Tables S4–S9).

269 **3.2. Data compilation: age estimation guidelines**

270 We distinguish between two sets of data with essentially different approaches for age estimation.
271 The ages of the first set, marked in gray in Fig. 6, were assigned by the excavators of the sites
272 using a complex body of archaeological evidence that does not include absolute radiocarbon ages
273 directly associated with the archaeointensity data. This raises two problems for paleomagnetists
274 and modelers. First, tracing back the considerations used to determine the ages requires specific
275 archaeological expertise, and, therefore, the quality, precision, and robustness of these ages
276 cannot be easily assessed without a detailed description of the age data. Second, in many cases,
277 the archaeological time scales, based on ceramic typology and cultural changes, might be loosely
278 linked to an absolute age scale and may have different age interpretations. Our approach in these

279 cases is to make as few changes as possible to the archaeological ages assigned by the excavators
 280 but rather to use wide age range that considers all possible correlations to the absolute age scale.

281 The ages of the color-coded datasets in Fig. 6 are assigned using radiocarbon or direct
 282 associations to historical events whose ages are considered consensuses by most of the
 283 archaeological community. The latter are significant for the time interval associated with the
 284 Hallstatt Plateau (ca. 800–400 BCE) in the radiocarbon calibration curve (Reimer et al., 2020).
 285 From the 8th to 6th century BCE, the ages are based on a correlation to two precisely-dated
 286 historical military campaigns described in the Hebrew Bible and other Mesopotamian texts -
 287 Assyrian (733–701 BCE) and Babylonian (600 – 586 BCE) – rather than on radiocarbon. In
 288 addition, the Aramean occupation (845–815 BCE), which is dated using both radiocarbon and
 289 historical constraints, is also used as a useful chronological tie point. The groups with age ranges
 290 tied to absolute ages are marked by four different colors in Fig. 6, and include the following
 291 datasets:

- 292 • The radiocarbon-dated stratigraphy of Tel Megiddo described in this study, which ended
 293 in the Assyrian destruction of the city.
- 294 • Two radiocarbon-dated layers from Tel Hazor (Stratum XVIII, Stratum XII) and a
 295 sequence of three stratigraphically ordered, short-lived phases from strata V-VI that
 296 ended in the Assyrian destruction of Hazor (Text S1, Tables S4-S5, supplementary
 297 material).
- 298 • A radiocarbon-dated sequence of ten slag layers from Timna-30. The Bayesian age model
 299 of the mound (Shaar et al., 2011), which was originally established using a
 300 magnetostratigraphic correlation with Khirbet en-Nahas (Ben-Yosef et al., 2009), is
 301 revised here to include only radiocarbon samples collected from Timna-30 (Text S2,
 302 Tables S6-S8, Supplementary Material)
- 303 • Materials dated by association to the Assyrian and Babylonian occupations or to the
 304 radiocarbon-dated Aramean campaign. This dataset includes 19 burnt structures (Vaknin
 305 et al., 2020; Vaknin et al., in press) and three groups of indicative ceramics that can be
 306 dated by association with cultural changes related to the occupations. The fired mud-
 307 brick structures found in the burnt level are crucial tie points for two reasons. First, as
 308 mentioned above, the uncertainty in radiocarbon dating in this period is in the order of
 309 200–400 years due to the plateau in the calibration curve, while the dates of the historical
 310 campaigns are unique in their precision. Second, the burnt bricks record a single event, as
 311 the fire during the destruction resets their magnetization, in contrast to pottery groups that
 312 provide data over a time interval representing a production period.

313 Supplementary Table S10 lists the VADM and the age range of 142 groups included in the
 314 LAC.v.1.0 compilation. We stress that none of the ages in the LAC data compilation were
 315 determined or constrained using archaeomagnetism in order to avoid circular reasoning.

316 **3.3. Bayesian modeling**

317 With the data described in Section 3.2 and listed in Supplementary Table S10, we calculate a
 318 Bayesian curve with its corresponding 95% credible envelope (Fig. 6, Supplementary Table
 319 S11). We term this curve ‘Levantine Archaeomagnetic Curve version 1.0’, or LAC.v.1.0. The
 320 LAC is calculated using the age hyperparameter reverse-jump Monte Carlo Markov Chain (AH-
 321 RJMCMC) algorithm developed by Livermore et al. (Livermore et al., 2018)
 322 (<https://github.com/plivermore/AH-RJMCMC1>). The algorithm is based on a piece-wise linear
 323 interpolation of the data between vertices drawn in a random-walk-like perturbation within a
 324 space allowed by the acceptance criteria. The prior assumptions of the model are: i) the allowed
 325 range of vertices’ VADM values is set to between 60 and 200 ZAm²; ii) the allowed number of
 326 vertices (K) is between K_{min} = 1 and K_{max} = 150; iii) ages in all contexts are uniformly
 327 distributed, except the ages of Timna, which were modeled as a normal distribution; and iv)
 328 group means and standard deviations define a normal distribution of the archaeointensity data. In
 329 addition, Supplementary Table S10 defines a stratigraphic order for contexts collected from the
 330 multi-layered sites (Tel Megiddo, Tel Hazor, Tell Atij, Tell Gudeda, Timna) and few mutual
 331 constraints between groups in Megiddo and Hazor. The AH-RJMCMC procedure takes into
 332 account all of these temporal relationships. The model uses the parameters $\sigma_{\text{move}} = 30 \text{ yrs}$, σ_{change}
 333 $= 10 \text{ Z Am}^2$, and $\sigma_{\text{birth}} = 10 \text{ Z Am}^2$, which define the random perturbation of a vertex in age, in
 334 intensity, and that of the linearly interpolated intensity value of a new vertex based on the current
 335 vertex distribution respectively. The age of a single datum is perturbed per age-resampling step
 336 ($\text{num_age_changes} = 1$); chain length is $2 \cdot 10^8$.

337 The sub-centennial resolution of the curve from 1100 to 550 BCE (encompassing the Levantine
 338 Iron Age anomaly) is achieved through several unique features of the combined datasets. Firstly,
 339 we obtained radiocarbon-dated contexts with age uncertainties of approximately a century and,
 340 in several cases, even less. Secondly, the stratigraphic relationships in Timna, Megiddo, and
 341 Hazor define constraints to the Bayesian model that lead to a reduction in the posterior age
 342 ranges. Lastly, we included data obtained from historically well-dated burnt levels and used a
 343 dense dataset with a large number of groups during the spike period.

344 4. Discussion

345 4.1 New constraints on the highest geomagnetic field intensity

346 Considering all the published paleointensity estimates from individual samples (i.e., not group
 347 means) from the past 5 My available in the GEOMAGIA50 v.3.3 (Brown et al., 2015) and PINT
 348 v.8.1.0 (Biggin et al., 2009; Bono et al., 2022) databases, only 1% of the data, which are
 349 sporadically scattered in time and space, show VADM > 150 ZAm². As such, VADM values
 350 calculated from global geomagnetic models do not exceed 140 ZAm² (e.g., Arneitz et al., 2019;
 351 Constable et al., 2016; Korte & Constable, 2018; Panovska et al., 2019; Pavon-Carrasco et al.,
 352 2014). The only exception is the time interval between the end of the 2nd millennium BCE and
 353 the middle of the 1st millennium BCE, where a number of archaeomagnetic observations point to
 354 high field values (>150 ZAm²) at several locations: the Levant (Ben-Yosef et al., 2017; Ertepinar
 355 et al., 2012; Shaar et al., 2011; Shaar et al., 2016; Vaknin et al., 2020), Caucasus (Shaar et al.,
 356 2017), China (Cai et al., 2017), Bulgaria (Kovacheva et al., 2014), Spain (Osete et al., 2020),
 357 Canary Islands (Kissel et al., 2015), Azores (Di Chiara et al., 2014) and Hawaii (Pressling et al.,
 358 2006). All these observations suggest short duration for the episodes of high intensity values.
 359 This behavior is probably associated with a more complex field structure than today’s (Korte &

360 Constable, 2018; Osete et al., 2020; Rivero-Montero et al., 2021) and, presumably, with a local
361 high field anomaly in the Near East, termed the ‘Levantine Iron Age Anomaly’ (LIAA) (Shaar et
362 al., 2018; Shaar et al., 2017; Shaar et al., 2016).

363 The highest VADM values during the climax of the LIAA were termed ‘geomagnetic spikes’ by
364 Ben-Yosef et al. (2009) and Shaar et al. (2011). Note that we use the term ‘spike’ hereafter in a
365 dual sense: first, to describe a short time interval (about a century long) with rates of intensity
366 change far exceeding those observed in the modern era (1840-2020), which would potentially
367 allow for other spikes to be observed outside of the LIAA, and second, to describe short-lived
368 intensity peaks exceeding the typical values in the geological record. Livermore et al. (2021)
369 questioned the robustness of the spikes and stated that the number of spikes and their values
370 strongly depend on the archaeomagnetic data used, particularly the experimental errors and the
371 averaging scheme adopted (i.e., sample groups versus individual samples). Here, we address the
372 issues raised by Livermore et al. (2021) and assemble a much denser dataset based solely on
373 group averages. This way, each data point in our compilation represents exactly the same
374 quantity and gains the same weight in the Bayesian calculation process. The new curve shows
375 the occurrence of four spikes with peak VADM of 155–162 $Z \text{ Am}^2$ around 1030, 840, 740, and
376 600 BCE. Each spike is represented by several coeval or nearly coeval groups, where overall,
377 fourteen groups have VADM > 150 $Z \text{ Am}^2$. Considering that each group represents a time
378 average of several samples, we suggest a value of 155 $Z \text{ Am}^2$ as a robust and conservative upper
379 limit for the maximum field value. Yet, based on sample data, higher values may have occurred
380 for short time intervals.

381

382 Fig. 7 demonstrates that spike-like values are rare in the paleomagnetic record, showing all the
383 published absolute paleointensity data with ages older than 1500 BCE from the GEOMAGIA50
384 and PINT databases. Only 49 data points out of 6816 have field values higher than 155 $Z \text{ Am}^2$,
385 none of which passes the rather strict statistical tests applied in the LAC. Given the specific
386 conditions associated with the Levantine geomagnetic spikes, the difficulty in detecting similar
387 high-paleointensity values in the global paleointensity record is understandable. First, our dense
388 dataset, including ten archaeointensity groups on average (each consisting of at least two
389 samples) per century during the LIAA interval (Fig. 6a) shows that the duration of the peaks is
390 around a century. Thus, if an average of few samples is required to obtain a robust paleointensity
391 estimate, a large dataset, such as the LAC compilation, is required to detect spikes. Second,
392 global geomagnetic models indicate that the geomagnetic dipole during the LIAA is most likely
393 the highest in the Holocene (Constable et al., 2016; Pavon-Carrasco et al., 2014; Schanner et al.,
394 2022). Thus, the likelihood of detecting spikes may depend on the likelihood that the ancient
395 paleomagnetic dipole was similarly high. Third, the spikes are a regional feature associated with
396 a local geomagnetic anomaly, expressed not only by high field values but also by directional
397 deviations from a dipole field (Osete et al., 2020; Shaar et al., 2018; Shaar et al., 2016).
398 Consequently, there are low chances that the scattered and sparse paleointensity database
399 spanning the geological record can reveal short-lived spikes. Moreover, from the comparison
400 with the global paleointensity database, we can conclude that spikes represent the highest value
401 the geomagnetic field can reach and can serve as a robust upper boundary for the maximum
402 strength of the geomagnetic field at a given location.

403

404

4.2 New constraints to maximum secular variation rates

405 The rates associated with the spikes range between $\sim 0.35 - 0.55 \mu\text{T}/\text{year}$ or $0.7 - 1.1 \text{ Z Am}^2/\text{year}$
406 in VADM values (Fig. 6c). To place these values within the context of the global geomagnetic
407 field behavior, we calculate in Fig. 8 the maximum rate in today's field by observing the
408 difference between IGRF models epochs 2015 and 2020 (Alken et al., 2021). For most of Earth's
409 surface, the rates do not exceed $0.1 \mu\text{T}/\text{year}$ ($\sim 0.2 \text{ Z Am}^2/\text{year}$), and a maximum rate of 0.12
410 $\mu\text{T}/\text{year}$ occurs only in limited areas (Fig. 8a). VADM transformation accounting for the
411 latitudinal dependency of the field yields a maximum rate of $0.25 \text{ Z Am}^2/\text{year}$ (Fig. 8b). We
412 expand the calculation back to 1840 using the *gufm1* model (Jackson et al., 2000) for 1840–1945
413 and the IGRF models for 1950–2020 (Alken et al., 2021) by looking at the maximum difference
414 in field intensity every five years at any point on Earth's surface. In our calculation we ignored
415 the interval 1945–1950 as we noticed an abrupt and very time-limited change in the rate at few
416 locations, which is likely an artifact caused by problematic global coverage of the data in the
417 1945 model. The maximum change rate in the past 190 years is not significantly different from
418 today, i.e., $0.18 \mu\text{T}/\text{year}$ or $0.33 \text{ Z Am}^2/\text{year}$. These rates are considerably lower than those
419 observed during the time intervals associated with geomagnetic spikes. Hence, LAC.v.1.0 also
420 places new robust constraints on how fast local field intensity can change.

421 We note that the rates calculated using LAC.v.1.0 appear more moderate than previously
422 considered (Ben-Yosef et al., 2009; Shaar et al., 2011), which had raised questions regarding the
423 dynamo processes behind them (Livermore et al., 2014; Troyano et al., 2020). Although the
424 spikes are now within the range of variations permitted by our current understanding of the
425 geodynamo (Davies & Constable, 2017; Davies & Constable, 2018; Livermore et al., 2014), the
426 fluctuations associated with the spikes remain unprecedented in their amplitude and rate.

427

4.3. Long-term evolution of the Levantine Iron Age Anomaly

428 The archeo-magnetostratigraphy of Tel Megiddo reveals the Holocene's greatest amplitude
429 change at multi-century scales between 1750 BCE and 1030 BCE. The increase began with a
430 minimum of 73 Z Am^2 in the 18th century BCE, a period characterized by the lowest intensities
431 in the Near East over the last five millennia, comparable to the low values at the beginning of the
432 3rd millennium BCE (Fig. 6b). The 700 year-long increase is nearly continuous, punctuated by a
433 century-scale peak around 1500 BCE. The spike period may, therefore, be a climax of a long-
434 term evolution in the geomagnetic field intensity in the Near East, which could result from the
435 occurrence of intense and rapidly evolving flux bundles at the core-mantle boundary. It also
436 contrasts with the period spanning from the 3rd millennium BCE to the 18th century BCE, which
437 shows intensity peaks of moderate amplitudes associated with lower change rates of less than 0.2
438 $\mu\text{T}/\text{year}$ (Figs. 6b,c; see also Gallet et al. (2020)). The significant increase in intensity would then
439 result in spikes instead of intensity peaks, with the first events also being shorter and apparently
440 more frequent, which could reflect a remarkable change in core dynamics.

441

5. Conclusions

442 We report here the largest archaeomagnetic intensity dataset currently available from a single
443 site, i.e. Tel Megiddo, with 23 sample groups collected from 18 consecutive radiocarbon-dated
444 archaeological strata.

445 We assemble a new archaeomagnetic compilation of the Levant and Upper Mesopotamia
446 between 3000 BCE to 550 BCE with 142 different groups of samples. The interval from 1700
447 BCE to 550 BCE is based mostly on contexts directly dated using radiocarbon and clear
448 associations with well-dated historical military campaigns, providing an unprecedented sub-
449 century resolution. We use this compilation to calculate the Levantine Archaeomagnetic Curve
450 (LAC.v.1.0), a Bayesian regional curve for high-precision archaeomagnetic dating.

451 The LAC depicts four geomagnetic spikes between 1050 BCE and 600 BCE, each lasting about a
452 century, defining new upper limits on both the maximum local field values and change rate.
453 Considering the overall uncertainty, we suggest 155 ZAm^2 and $0.5 \mu\text{T/year}$ ($1.0 \text{ ZAm}^2/\text{year}$ in
454 VADM values) as conservative upper boundaries for these quantities.

455 As a concluding remark, we highlight the challenge in constructing a robust, continuous
456 geomagnetic intensity curve at a sub-centennial resolution over a large millennial time scales.
457 This is made possible in this study by exploiting the advantage of the Near East's abundance of
458 data that allows acquisition of large multiple archaeomagnetic datasets with precise dating,
459 stratigraphic constraints, and cross-correlations between sites. In this respect, Tel Megiddo is an
460 exemplary case study demonstrating a strong link between archaeology, radiocarbon, and
461 geomagnetism.

462 **Acknowledgments**

463 This project has received funding from the European Research Council (ERC) under the
464 European Union's Horizon 2020 research and innovation programme (grant agreement No
465 804490) to RS. The study was partly supported by the Israel Science Foundation (ISF) grant
466 1364/15 to RS. It was partly financed by the INSU-CNRS program PNP to YG. Work on the
467 Megiddo samples was supported by the Dan David Foundation and grants from Mark Weissman
468 and Jacques Chahine to IF. We thank Phil Livermore for assisting with the AH-RJMCMC
469 analysis. We thank Maxwell Brown and the anonymous reviewer whose constructive comments
470 helped improve the manuscript.

471

472 **Open Research**

473 All measurement data are available in the MagIC database (earthref.org/MagIC/19395).

474

475

476 **References**

- 477 Alken, P., Thebault, E., Beggan, C. D., Amit, H., Aubert, J., Baerenzung, J., et al. (2021). International
478 Geomagnetic Reference Field: the thirteenth generation. *Earth Planets and Space*, 73(1)
479 <https://doi.org/10.1186/s40623-020-01288-x>
- 480 Arneitz, P., Egli, R., Leonhardt, R., & Fabian, K. (2019). A Bayesian iterative geomagnetic model with
481 universal data input: Self-consistent spherical harmonic evolution for the geomagnetic field over
482 the last 4000 years. *Physics of the Earth and Planetary Interiors*, 290, 57-75
483 <https://doi.org/10.1016/j.pepi.2019.03.008>

- 484 Arneitz, P., Leonhardt, R., Schnepf, E., Heilig, B., Mayrhofer, F., Kovacs, P., et al. (2017). The
485 HISTMAG database: combining historical, archaeomagnetic and volcanic data. *Geophysical*
486 *Journal International*, 210(3), 1347-1359 <https://doi.org/10.1093/gji/ggx245>
- 487 Ben-Yosef, E., Millman, M., Shaar, R., Tauxe, L., & Lipschits, O. (2017). Six centuries of geomagnetic
488 intensity variations recorded by royal Judean stamped jar handles. *Proceedings of the National*
489 *Academy of Sciences of the United States of America*, 114(9), 2160-2165
490 <https://doi.org/10.1073/pnas.1615797114>
- 491 Ben-Yosef, E., Tauxe, L., Levy, T. E., Shaar, R., Ron, H., & Najjar, M. (2009). Geomagnetic intensity
492 spike recorded in high resolution slag deposit in Southern Jordan. *Earth and Planetary Science*
493 *Letters*, 287(3-4), 529-539 <https://doi.org/10.1016/j.epsl.2009.09.001>
- 494 Biggin, A. J., Strik, G. H. M. A., & Langereis, C. G. (2009). The intensity of the geomagnetic field in the
495 late-Archaean: new measurements and an analysis of the updated IAGA palaeointensity database.
496 *Earth Planets and Space*, 61(1), 9-22 <https://doi.org/10.1186/Bf03352881>
- 497 Boaretto, E. (2022). Radiocarbon dating. In M. A. S. Martin & I. Finkelstein (Eds.), *Megiddo VI: The*
498 *2010-2014 Seasons*. PA: State College.
- 499 Bono, R. K., Paterson, G. A., van der Boon, A., Engbers, Y. A., Grappone, J. M., Handford, B., et al.
500 (2022). The PINT database: a definitive compilation of absolute palaeomagnetic intensity
501 determinations since 4 billion years ago. *Geophysical Journal International*, 229(1), 522-545
502 <https://doi.org/10.1093/gji/ggab490>
- 503 Brown, M. C., Donadini, F., Korte, M., Nilsson, A., Korhonen, K., Lodge, A., et al. (2015).
504 GEOMAGIA50.v3: 1. general structure and modifications to the archeological and volcanic
505 database. *Earth Planets and Space*, 67, 1-31 <https://doi.org/10.1186/s40623-015-0232-0>
- 506 Brown, M. C., Herve, G., Korte, M., & Genevey, A. (2021). Global archaeomagnetic data: The state of
507 the art and future challenges. *Physics of the Earth and Planetary Interiors*, 318
508 <https://doi.org/10.1016/j.pepi.2021.106766>
- 509 Cai, S. H., Jin, G. Y., Tauxe, L. S., Deng, C. L., Qin, H. F., Pan, Y. X., & Zhu, R. X. (2017).
510 Archaeointensity results spanning the past 6 kiloyears from eastern China and implications for
511 extreme behaviors of the geomagnetic field. *Proceedings of the National Academy of Sciences of*
512 *the United States of America*, 114(1), 39-44 <https://doi.org/10.1073/pnas.1616976114>
- 513 Campuzano, S. A., Gomez-Paccard, M., Pavon-Carrasco, F. J., & Osete, M. L. (2019). Emergence and
514 evolution of the South Atlantic Anomaly revealed by the new paleomagnetic reconstruction
515 SHAWQ2k. *Earth and Planetary Science Letters*, 512, 17-26
516 <https://doi.org/10.1016/j.epsl.2019.01.050>
- 517 Coe, R., Gromme, S., & Mankinen, E. (1978). Geomagnetic paleointensities from radiocarbon-dated lava
518 flows on Hawaii and question of Pacific nondipole low. *Journal of Geophysical Research*, 1740-
519 1756 <https://doi.org/10.1029/JB083iB04p01740>
- 520 Constable, C., Korte, M., & Panovska, S. (2016). Persistent high paleosecular variation activity in
521 southern hemisphere for at least 10 000 years. *Earth and Planetary Science Letters*, 453, 78-86
522 <https://doi.org/10.1016/j.epsl.2016.08.015>
- 523 Courtillot, V., & Le Mouel, J. L. (2007). The study of earth's magnetism (1269-1950): A foundation by
524 peregrinus and subsequent development of geomagnetism and paleomagnetism. *Reviews of*
525 *Geophysics*, 45(3) <https://doi.org/10.1029/2006rg000198>
- 526 Davies, C., & Constable, C. (2017). Geomagnetic spikes on the core-mantle boundary. *Nature*
527 *Communications*, 8 <https://doi.org/10.1038/ncomms15593>
- 528 Davies, C. J., & Constable, C. G. (2018). Searching for geomagnetic spikes in numerical dynamo
529 simulations. *Earth and Planetary Science Letters*, 504, 72-83
530 <https://doi.org/10.1016/j.epsl.2018.09.037>
- 531 Di Chiara, A., Tauxe, L., & Speranza, F. (2014). Paleointensity determination from Sao Miguel (Azores
532 Archipelago) over the last 3 ka. *Physics of the Earth and Planetary Interiors*, 234, 1-13
533 <https://doi.org/10.1016/j.pepi.2014.06.008>

- 534 Ertepinar, P., Langereis, C. G., Biggin, A. J., Frangipane, M., Matney, T., Okse, T., & Engin, A. (2012).
 535 Archaeomagnetic study of five mounds from Upper Mesopotamia between 2500 and 700 BCE:
 536 Further evidence for an extremely strong geomagnetic field ca. 3000 years ago. *Earth and*
 537 *Planetary Science Letters*, 357, 84-98 <https://doi.org/10.1016/j.epsl.2012.08.039>
- 538 Finkelstein, I. (2009). Destructions: Megiddo as a case study. In J. D. Schloen (Ed.), *Exploring the*
 539 *Longue Durée* (pp. 113-126). Indiana: Eisenbrauns.
- 540 Gallet, Y., & Al-Maqdissi, M. (2010). Archeomagnetism in Mishirfeh-Qatna: New data on the evolution
 541 of intensity in the earthly magnetic field in the Middle East during the last millenia. *Akkadica*,
 542 131(1), 29-46
- 543 Gallet, Y., & Butterlin, P. (2015). Archaeological and geomagnetic implications of new archaeomagnetic
 544 intensity data from the Early Bronze High Terrace 'Massif Rouge' at Mari (Tell Hariri, Syria).
 545 *Archaeometry*, 57, 263-276 <https://doi.org/10.1111/arc.12112>
- 546 Gallet, Y., D'Andrea, M., Genevey, A., Pinnock, F., Le Goff, M., & Matthiae, P. (2014).
 547 Archeomagnetism at Ebla (Tell Mardikh, Syria). New data on geomagnetic field intensity
 548 variations in the Near East during the Bronze Age. *Journal of Archaeological Science*, 42, 295-
 549 304 <https://doi.org/10.1016/j.epsl.2017.11.013>
- 550 Gallet, Y., Fortin, M., Fournier, A., Le Goff, M., & Livermore, P. (2020). Analysis of geomagnetic field
 551 intensity variations in Mesopotamia during the third millennium BC with archeological
 552 implications. *Earth and Planetary Science Letters*, 537
 553 <https://doi.org/10.1016/j.epsl.2020.116183>
- 554 Gallet, Y., Genevey, A., Le Goff, M., Fluteau, F., & Ali Eshraghi, S. (2006). Possible impact of the
 555 Earth's magnetic field on the history of ancient civilizations. *Earth and Planetary Science Letters*,
 556 246(1-2), 17-26 <https://doi.org/10.1016/j.epsl.2006.04.001>
- 557 Gallet, Y., & Le Goff, M. (2006). High-temperature archeointensity measurements from Mesopotamia.
 558 *Earth and Planetary Science Letters*, 241(1-2), 159-173
 559 <https://doi.org/10.1016/j.epsl.2005.09.058>
- 560 Gallet, Y., Le Goff, M., Genevey, A., Margueron, J., & Matthiae, P. (2008). Geomagnetic field intensity
 561 behavior in the Middle East between similar to 3000 BC and similar to 1500 BC. *Geophysical*
 562 *Research Letters*, 35(2) <https://doi.org/10.1029/2007gl031991>
- 563 Garcia, R., Perez-Rodriguez, N., Goguitchaichvili, A., Ceja, M. R., Morales, J., Soler, A. M., & Urrutia-
 564 Fucugauchi, J. (2021). On the absolute geomagnetic intensity fluctuations in Mexico over the last
 565 three millennia. *Journal of South American Earth Sciences*, 106 <https://doi.org/ARTN 102927>
 566 10.1016/j.jsames.2020.102927
- 567 Genevey, A., Gallet, Y., Thebault, E., Livermore, P. W., Fournier, A., Jesset, S., et al. (2021).
 568 Archeomagnetic intensity investigations of French medieval ceramic workshops: Contribution to
 569 regional field modeling and archeointensity-based dating. *Physics of the Earth and Planetary*
 570 *Interiors*, 318
- 571 Genevey, A., Gallet, Y., Constable, C. G., Korte, M., & Hulot, G. (2008). ArcheoInt: An upgraded
 572 compilation of geomagnetic field intensity data for the past ten millennia and its application to the
 573 recovery of the past dipole moment. *Geochemistry Geophysics Geosystems*, 9 [https://doi.org/Artn](https://doi.org/Artn Q04038)
 574 Q04038
 575 10.1029/2007gc001881
- 576 Genevey, A., Gallet, Y., Jesset, S., Thebault, E., Bouillon, J., Lefevre, A., & Le Goff, M. (2016). New
 577 archeointensity data from French Early Medieval pottery production (6th-10th century AD).
 578 Tracing 1500 years of geomagnetic field intensity variations in Western Europe. *Physics of the*
 579 *Earth and Planetary Interiors*, 257, 205-219
- 580 Genevey, A. S., Gallet, Y., & Margueron, J. C. (2003). Eight thousand years of geomagnetic field
 581 intensity variations in the eastern Mediterranean. *Journal of Geophysical Research-Solid Earth*,
 582 108(B5) <https://doi.org/10.1029/2001jb001612>
- 583 Jackson, A., Jonkers, A. R. T., & Walker, M. R. (2000). Four centuries of geomagnetic secular variation
 584 from historical records. *Philosophical Transactions of the Royal Society of London Series a-*

- 585 *Mathematical Physical and Engineering Sciences*, 358(1768), 957-990
586 <https://doi.org/10.1098/rsta.2000.0569>
- 587 Kirschvink, J. L. (1980). The Least-Squares Line and Plane and the Analysis of Paleomagnetic Data.
588 *Geophysical Journal of the Royal Astronomical Society*, 62(3), 699-718
589 <https://doi.org/10.1111/j.1365-246X.1980.tb02601.x>
- 590 Kissel, C., Laj, C., Rodriguez-Gonzalez, A., Perez-Torrado, F., Carracedo, J. C., & Wandres, C. (2015).
591 Holocene geomagnetic field intensity variations: Contribution from the low latitude Canary
592 Islands site. *Earth and Planetary Science Letters*, 430, 178-190
593 <https://doi.org/10.1016/j.epsl.2015.08.005>
- 594 Korte, M., & Constable, C. G. (2018). Archeomagnetic Intensity Spikes: Global or Regional
595 Geomagnetic Field Features? *Frontiers in Earth Science*, 6
596 <https://doi.org/10.3389/feart.2018.00017>
- 597 Kovacheva, M., Kostadinova-Avramova, M., Jordanova, N., Lanos, P., & Boyadzhiev, Y. (2014).
598 Extended and revised archaeomagnetic database and secular variation curves from Bulgaria for
599 the last eight millennia. *Physics of the Earth and Planetary Interiors*, 236, 79-94
- 600 Le Goff, M., & Gallet, Y. (2004). A new three-axis vibrating sample magnetometer for continuous high-
601 temperature magnetization measurements: applications to paleo- and archeo-intensity
602 determinations. *Earth and Planetary Science Letters*, 229(1-2), 31-43
603 <https://doi.org/10.1016/j.epsl.2004.10.025>
- 604 Livermore, P. W., Fournier, A., & Gallet, Y. (2014). Core-flow constraints on extreme archeomagnetic
605 intensity changes. *Earth and Planetary Science Letters*, 387, 145-156
606 <https://doi.org/10.1016/j.epsl.2013.11.020>
- 607 Livermore, P. W., Fournier, A., Gallet, Y., & Bodin, T. (2018). Transdimensional inference of
608 archeomagnetic intensity change. *Geophysical Journal International*, 215(3), 2008-2034
609 <https://doi.org/10.1093/gji/ggy383>
- 610 Livermore, P. W., Gallet, Y., & Fournier, A. (2021). Archeomagnetic intensity variations during the era
611 of geomagnetic spikes in the Levant. *Physics of the Earth and Planetary Interiors*, 312
612 <https://doi.org/10.1016/j.pepi.2021.106657>
- 613 Martin, M. A. S., Finkelstein, I., & Piasetzky, E. (2020). Radiocarbon-dating the Late Bronze Age:
614 Cultural and historical considerations on Megiddo and beyond. *Bulltin of the American Schools of*
615 *Oriental Research*, 384 <https://doi.org/10.1086/709576>
- 616 Nilsson, A., Holme, R., Korte, M., Suttie, N., & Hill, M. (2014). Reconstructing Holocene geomagnetic
617 field variation: new methods, models and implications. *Geophysical Journal International*,
618 198(1), 229-248 <https://doi.org/10.1093/gji/ggu120>
- 619 Nilsson, A., Suttie, N., Stoner, J. S., & Muscheler, R. (2022). Recurrent ancient geomagnetic field
620 anomalies shed light on future evolution of the South Atlantic Anomaly. *Proceedings of the*
621 *National Academy of Sciences*, 119(24), e2200749119
622 <https://doi.org/doi:10.1073/pnas.2200749119>
- 623 Osete, M. L., Molina-Cardin, A., Campuzano, S. A., Aguilera-Arzo, G., Barrachina-Ibanez, A., Falomir-
624 Granell, F., et al. (2020). Two archaeomagnetic intensity maxima and rapid directional variation
625 rates during the Early Iron Age observed at Iberian coordinates. Implications on the evolution of
626 the Levantine Iron Age Anomaly. *Earth and Planetary Science Letters*, 533
627 <https://doi.org/10.1016/j.epsl.2019.116047>
- 628 Panovska, S., Korte, M., & Constable, C. G. (2019). One hundred thousand years of geomagnetic field
629 evolution. *Reviews of Geophysics*, 57(4), 1289-1337 <https://doi.org/10.1029/2019rg000656>
- 630 Paterson, G. A., Tauxe, L., Biggin, A. J., Shaar, R., & Jonestrask, L. C. (2014). On improving the
631 selection of Thellier-type paleointensity data. *Geochemistry Geophysics Geosystems*, 15(4), 1180-
632 1192 <https://doi.org/10.1002/2013gc005135>
- 633 Pavon-Carrasco, F. J., Osete, M. L., Torta, J. M., & De Santis, A. (2014). A geomagnetic field model for
634 the Holocene based on archaeomagnetic and lava flow data. *Earth and Planetary Science Letters*,
635 388, 98-109 <https://doi.org/10.1016/j.epsl.2013.11.046>

- 636 Pressling, N., Laj, C., Kissel, C., Champion, D., & Gubbins, D. (2006). Palaeomagnetic intensities from
637 C-14-dated lava flows on the Big Island, Hawaii: 0-21 kyr. *Earth and Planetary Science Letters*,
638 247(1-2), 26-40 <https://doi.org/10.1016/j.epsl.2006.04.026>
- 639 Regev, J., Finkelstein, I., Adams, M. J., & E., B. (2014). Wiggled-matched 14C chronology of Early
640 Bronze Megiddo and the synchronization of Egyptian and Levantine chronologies. *Egypt and the*
641 *Levant* 24, 241-264
- 642 Reimer, P. J., Austin, W. E. N., Bard, E., Bayliss, A., Blackwell, P. G., Ramsey, C. B., et al. (2020). The
643 Intcal20 Northern hemisphere radiocarbon age calibration curve (0-55 Cal Kbp). *Radiocarbon*,
644 62(4), 725-757 <https://doi.org/10.1017/Rdc.2020.41>
- 645 Rivero-Montero, M., Gomez-Paccard, M., Pavon-Carrasco, F. J., Cau-Ontiveros, M. A., Fantuzzi, L.,
646 Martin-Hernandez, F., et al. (2021). Refining geomagnetic field intensity changes in Europe
647 between 200 CE and 1800 CE. New data from the Mediterranean region. *Physics of the Earth and*
648 *Planetary Interiors*, 317 <https://doi.org/ARTN 106749>
649 10.1016/j.pepi.2021.106749
- 650 Schanner, M., Korte, M., & Holschneider, M. (2022). ArchKalmag14k: A Kalman-Filter Based Global
651 Geomagnetic Model for the Holocene. *Journal of Geophysical Research-Solid Earth*, 127(2)
652 <https://doi.org/10.1029/2021JB023166>
- 653 Schnepf, E., Thallner, D., Arneitz, P., & Leonhardt, R. (2020). New archeomagnetic secular variation
654 data from Central Europe, II: Intensities. *Physics of the Earth and Planetary Interiors*, 309
655 <https://doi.org/ARTN 106605>
656 10.1016/j.pepi.2020.106605
- 657 Selkin, P. A., & Tauxe, L. (2000). Long-term variations in palaeointensity. *Philosophical Transactions of*
658 *the Royal Society a-Mathematical Physical and Engineering Sciences*, 358(1768), 1065-1088
659 <https://doi.org/10.1098/rsta.2000.0574>
- 660 Shaar, R., Bechar, S., Finkelstein, I., Gallet, Y., Martin, M. A. S., Ebert, Y., et al. (2020). Synchronizing
661 Geomagnetic Field Intensity Records in the Levant Between the 23rd and 15th Centuries BCE:
662 Chronological and Methodological Implications. *Geochemistry Geophysics Geosystems*, 21(12)
663 <https://doi.org/10.1029/2020GC009251>
- 664 Shaar, R., Ben-Yosef, E., Ron, H., Tauxe, L., Agnon, A., & Kessel, R. (2011). Geomagnetic field
665 intensity: How high can it get? How fast can it change? Constraints from Iron Age copper slag.
666 *Earth and Planetary Science Letters*, 301(1-2), 297-306
667 <https://doi.org/10.1016/j.epsl.2010.11.013>
- 668 Shaar, R., Hassul, E., Raphael, K., Ebert, Y., Segal, Y., Eden, I., et al. (2018). The first catalog of
669 archaeomagnetic directions from Israel with 4,000 years of geomagnetic secular variations.
670 *Frontiers in Earth Science*, 6 <https://doi.org/10.3389/feart.2018.00164>
- 671 Shaar, R., & Tauxe, L. (2013). Thellier GUI: An integrated tool for analyzing paleointensity data from
672 Thellier-type experiments. *Geochemistry Geophysics Geosystems*, 14(3), 677-692
673 <https://doi.org/10.1002/ggge.20062>
- 674 Shaar, R., Tauxe, L., Ben-Yosef, E., Kassianidou, V., Lorentzen, B., Feinberg, J. M., & Levy, T. E.
675 (2015). Decadal-scale variations in geomagnetic field intensity from ancient Cypriot slag
676 mounds. *Geochemistry Geophysics Geosystems*, 16(1), 195-214
677 <https://doi.org/10.1002/2014gc005455>
- 678 Shaar, R., Tauxe, L., Goguitchaichvili, A., Devidze, M., & Licheli, V. (2017). Further evidence of the
679 Levantine Iron Age geomagnetic anomaly from Georgian pottery. *Geophysical Research Letters*,
680 44(5), 2229-2236 <https://doi.org/10.1002/2016gl071494>
- 681 Shaar, R., Tauxe, L., Ron, H., Ebert, Y., Zuckerman, S., Finkelstein, I., & Agnon, A. (2016). Large
682 geomagnetic field anomalies revealed in Bronze to Iron Age archeomagnetic data from Tel
683 Megiddo and Tel Hazor, Israel. *Earth and Planetary Science Letters*, 442, 173-185
684 <https://doi.org/10.1016/j.epsl.2016.02.038>
- 685 Tauxe, L., Shaar, R., Jonestrask, L., Swanson-Hysell, N. L., Minnett, R., Koppers, A. A. P., et al. (2016).
686 PmagPy: Software package for paleomagnetic data analysis and a bridge to the Magnetics

- 687 Information Consortium (MagIC) Database. *Geochemistry Geophysics Geosystems*, 17(6), 2450-
688 2463 <https://doi.org/10.1002/2016gc006307>
- 689 Tauxe, L., & Staudigel, H. (2004). Strength of the geomagnetic field in the Cretaceous Normal
690 Superchron: New data from submarine basaltic glass of the Troodos Ophiolite. *Geochemistry
691 Geophysics Geosystems*, 5 <https://doi.org/10.1029/2003GC000635>
- 692 Toffolo, M. B., Arie, E., Martin, M. A. S., Boaretto, E., & Finkelstein, I. (2014). Absolute chronology of
693 Megiddo, Israel, in the Late Bronze and Iron Ages: High-resolution radiocarbon dating.
694 *Radiocarbon*, 56(1), 221-244 <https://doi.org/10.2458/56.16899>
- 695 Troyano, M., Fournier, A., Gallet, Y., & Finlay, C. C. (2020). Imprint of magnetic flux expulsion at the
696 core-mantle boundary on geomagnetic field intensity variations. *Geophysical Journal
697 International*, 221(3), 1984-2009 <https://doi.org/10.1093/gji/ggaa126>
- 698 Vaknin, Y., Shaar, R., Gadot, Y., Shalev, Y., Lipschits, O., & Ben-Yosef, E. (2020). The Earth's magnetic
699 field in Jerusalem during the Babylonian destruction: A unique reference for field behavior and
700 an anchor for archaeomagnetic dating. *Plos One*, 15(8)
701 <https://doi.org/10.1371/journal.pone.0237029>
- 702 Vaknin, Y., Shaar, R., Lipschits, O., Mazar, A., Maeir, A., Garfinkel, Y., et al. (in press). Reconstructing
703 biblical military campaigns using geomagnetic field data *Proceedings of the National Academy of
704 Sciences*
- 705 Yu, Y. J., Tauxe, L., & Genevey, A. (2004). Toward an optimal geomagnetic field intensity determination
706 technique. *Geochemistry Geophysics Geosystems*, 5 <https://doi.org/10.1029/2003gc000630>
707
708

709 **Table 1: Acceptance criteria, LAC.v.1.0**

Criteria group *	Statistic	Threshold value	Description	Reference †
Specimen	FRAC	0.79	Fraction parameter	Shaar and Tauxe (2013)
	B	0.1	Scatter parameter	Coe et al. (1978); Selkin and Tauxe (2000)
	SCAT	True	Scatter parameter	Shaar and Tauxe (2013)
	GAP-MAX	0.5	Maximum gap	Shaar and Tauxe (2013)
	N_{PTRM}	2	Number of pTRM checks	
	N	5	Number of data points	
	MAD	5	Maximum Angular Deviation of the zero field steps	Kirschvink (1980)
	DANG	10	Deviation Angle	Tauxe and Staudigel (2004)
Alteration check (correction)	6%	Alteration check in TRM anisotropy and cooling rate experiments	Shaar et al. (2015)	
Sample (pottery vessel, furnace, brick, slag)	N_{min}	3	Number of specimens	
	$N_{\text{min_aniso_corr}}$	at least half of the specimens	Minimum number of specimens with anisotropy correction	
	$N_{\text{min_cr_corr}}$	1	Minimum number of specimens with cooling rate correction	
	Σ	$\sigma < 3 \mu\text{T}$ OR $\sigma \% < 8\%$	Standard deviation of the sample mean	
	Anisotropy sample test	6%	If the mean anisotropy correction of all the specimens from the same sample (fragment) is higher than this value, specimens without anisotropy correction are discarded	

710 * For a complete description and definitions of paleointensity statistics, see Paterson et al. (2014).

711

712 **Table 2: Archaeointensity results in Tel Megiddo.**

Megiddo Group	Name in LAC.v.1.0*	Published radiocarbon age range 68.2% probability interval (95.4 % probability interval) (BCE)†	Age range in LAC.v.1.0 compilation (BCE) ‡	N samples	n specimens	B (μT)	B σ (μT)	VADM (ZAm ²)	VADM σ (ZAm ²)
Q-2	mgq02	801-756 (805-735); Assyrian destruction level	820-732	4	15	74.6	3.6	140.3	6.9
H-3-low	mgh03-low	-	820-732	7	37	76.7	3.7	144.3	6.9
H-3-high	mgh03-high			4	18	89.6	2.7	168.6	5.1
Q-4	mgq04	897-821 (901-809)	890-840	3	14	76.4	1.7	143.7	3.1
Q-5	mgq05	956-894 (967-848)	925-875	6	30	69	3.8	129.8	7.1
H-7	Mgh07	930-900 (945-860)	925-875	3	16	71.8	3.7	135.1	6.9
Q-6	mgq06	979-911 (989-876)	950-900	4	16	64.6	3.2	121.5	6
Q-7	mgq07	1047-975 (1052-946)	1050-950	6	18	71	2.7	133.5	5.1
H-9-low	mgh09-low	1038-976 (1056-936)	1050-950	3	15	69.1	4	129.9	7.5
H-9-high	mgh09-high			2	9	83.2	0.4	156.5	0.7
K-4	mgk04	1037-951 (1053-908)	1050-950	4	15	75.5	4.9	142	9.1
H-10	mgh10	1068-1031 (1087-1023)	1100-1025	5	15	69.7	4.3	131	8.1
H-11	mgh11	1105-1051 (1115-1041)	1125-1075	10	30	69.7	4.8	131.1	9.1
K-6	mgk06	1148-1123 (1168-1104)	1175-1125	7	31	64.2	2.6	120.8	4.9
K-8	mgk08	1238-1178 (1268-1158)	1250-1175	8	33	57.3	3.2	107.8	6
K-9	mgk09	1323-1230 (1381-1201)	1400-1250	6	20	54.2	2.2	102	4.1

F-10	mgf10	1545-1354 (1561-1313)	1550-1400	3	14	50.6	1.3	95.2	2.5
H-15	mgh15	1557-1509 (1572-1463)	1550-1475	5	25	54.9	4.3	103.3	8
K-10	mgk10	1581-1545 (1596-1535)	1600-1550	8	35	52.2	5.7	98.2	10.7
K-11	mgk11	1626-1579 (1643-1561)	1650-1600	4	21	52.2	4.5	98.2	8.4
F-13	mgf13	-	1900-1700	4	25	42	2.5	78.9	4.6
S-3	mgs03	1942-1902 (1965-1886)	1950-1900	4	12	38.8	3.5	72.9	6.6
J-6	mgj06	2860-2540 (2880-2450)	2850-2500	4	15	39	0.9	73.4	1.8
J-5	mgj05	2920-2720 (2970-2670)	2900-2800	4	12	44.2	4.3	83.2	8
J-4 §	mgj04	3060-2880 (3180-2830)	3100-2900	8	46	41.1	7.1	77.3	13.3
J-4a §	mgj04a	3060-2880 (3180-2830)	3100-2900	3	10	40.1	1.6	75.4	3.1

713 * Name in model data (Supplementary Table S10)

714 † Radiocarbon data from Regev et al. (2014); Toffolo et al. (2014); Martin et al. (2020); Boaretto (2022); There are
715 no radiocarbon data from H-03, and the age is linked to the Assyrian destruction level. Ages from S-3 are
716 preliminary. There are no radiocarbon data from F-13, and the age is inferred from correlation to strata in areas K
717 and S.

718 ‡ Age range used in the archaeomagnetic compilation and in Bayesian modelling.

719 § J-4 and J-4a are two groups from the same level. J-4a fragments were collected from loci representing the final
720 days of the temple, whereas the J-4 items originated from a fill context.

721

722 Figure 1: Map showing Tel Megiddo and other sites in the Levant and Western Upper
 723 Mesopotamia used to construct the Levantine Archaeomagnetic Curve (LAC.v.1.0) shown in
 724 Fig. 6. Color code is as in Fig. 6.

725 Figure 2: Tel Megiddo. a) Aerial photo of the mound displaying the excavation areas discussed
 726 in the text. b) Tel Megiddo stratigraphy showing all the contexts analyzed for archaeointensity.
 727 The shaded cells mark destruction layers.

728 Figure 3: Representative results of specimen analysis conducted in this study. (a–d) Red (blue)
 729 circles, and triangles in the main Arai plots are ZI steps, IZ steps, and pTRM checks,
 730 respectively. Heating temperatures (C°) are displayed near the symbols. Blue (red) squares in the
 731 inset Zijdeveld plots are x-y (x-z) projections of the remaining NRM, where the x-axis is
 732 rotated to the direction of the NRM. The green line is the best fit. a) Specimen passing all
 733 criteria. b–d) Interpretations failing the SCAT (b), FRAC (c), and MAD+DANG (d) criteria. e) A
 734 successful cooling rate experiment. Blue circles are four measurements at three different cooling
 735 rates, and the red square is a projection of the ancient cooling rate on the best-fit (dashed line).

736 Figure 4: Histograms of anisotropy and cooling rate corrections.

737 Figure 5: Archaeomagnetic stratigraphy of Tel Megiddo constructed from 132 samples. Full
 738 circles (red squares) represent the archaeointensity of samples (group means). Number of
 739 samples used to calculate the group means is indicated above each error bar. Vertical lines
 740 represent chrono-stratigraphic division. Fragment (sample) groups are plotted according to their
 741 relative age.

742 Figure 6: An archaeointensity curve. a, b) Levantine Archaeomagnetic Intensity Curve
 743 (LAC.v.1.0). Colored symbols are groups of samples directly dated with radiocarbon or by clear
 744 association with dated historical events. Gray symbols represent groups dated using various
 745 archaeological methods. From the 17th to the 6th centuries, there is at least one directly-dated
 746 context per century. Curve and shaded area in (a–b) are the average and the 95% credible
 747 interval calculated using the AH-RJMCMC algorithm (Livermore et al., 2018), respectively. c)
 748 Rate of change. Dashed red and dotted orange lines show the maximum rate for 1840–2020 and
 749 the maximum rate in today's field (Fig. 7), respectively. The oscillation pattern revealed in (a)
 750 includes four spikes with VADM >150 ZAm² and a change rate of 0.35–0.55 μ T/year (0.7–1.1
 751 ZAm²) (c).

752 Figure 7: Comparison of spikes' paleointensity with the global databases. a) PINT v.8.1.0
 753 database (Bono et al., 2022). b) GEOMAGIA50 v.3.3 (Brown et al., 2015) before 3500 yBP.
 754 Horizontal lines show the value of 155 ZAm² corresponding to the spike with the lowest
 755 intensity maximum according to LAC.v.1.0 (Fig. 6). N is the number of paleointensity estimates
 756 below and above 155 ZAm².

757 Figure 8: Maximum change rate of the geomagnetic field intensity for 1840–2020. a–b) Intensity
 758 and VADM rate of change in today's field, calculated using the IGRF13 model (Alken et al.,
 759 2021) epochs 2015–2020. c–d) Maximum intensity and VADM rate of change for 1840–2020,
 760 calculated using the IGRF models (Alken et al., 2021) between 1950–2020 and the gufm1 model
 761 (Jackson et al., 2000) between 1840–1950. e) Field intensity and rate of change at the location

762 with the maximum B change (40°S, 45°E). f) VADM and rate of change at the location with the
763 maximum VADM change (20°N, 65°W).

Figure 1.

a)

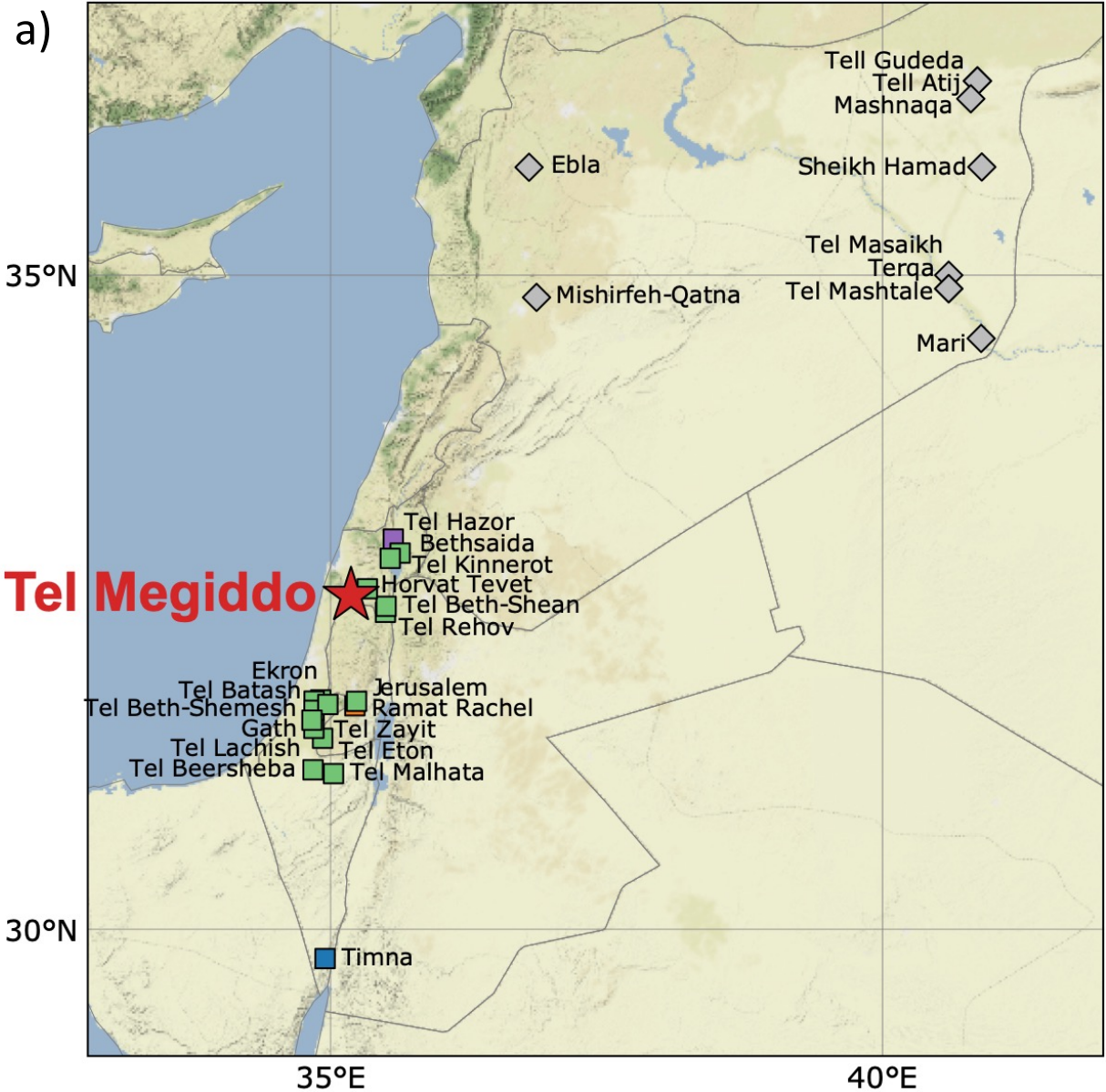
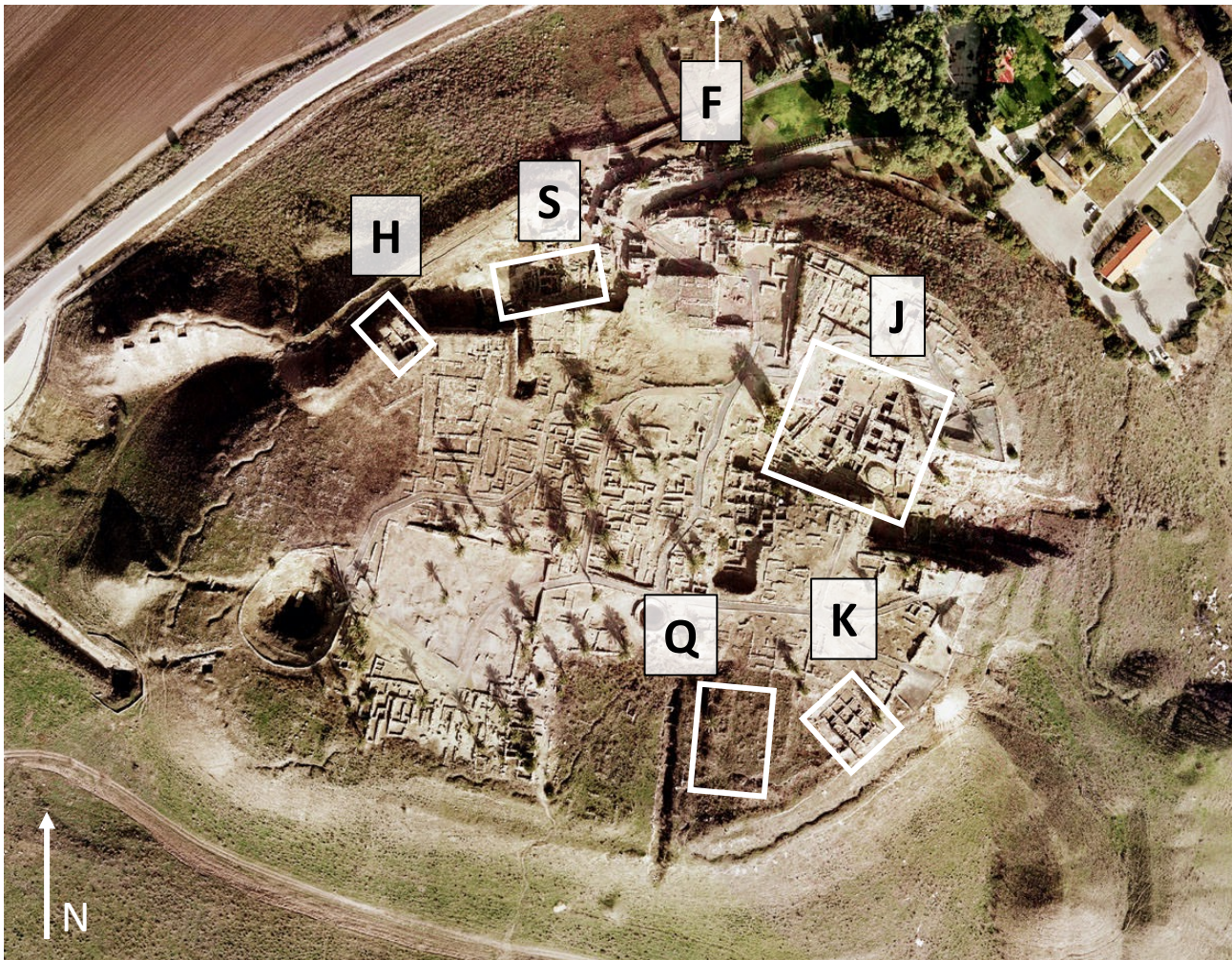


Figure 2.

a)



b)

Area	J	S	F	K	H	Q
Period						
Early Iron IIB					H-3	Q-2
Late Iron IIA						Q-4
Middle Iron IIA					H-7	Q-5
Early Iron IIA						Q-6
Late Iron I				K-4	H-9	Q-7
Middle Iron I					H-10	
Early Iron I					H-11	
Late Bronze III				K-6		
Late Bronze IIB				K-8		
Late Bronze IIA-IIB				K-9		
Late Bronze I			F-10		H-15	
Middle Bronze III				K-10		
Middle Bronze III				K-11		
Middle Bronze II			F-13			
Middle Bronze I		S-3				
Early Bronze III	J-6					
Early Bronze III	J-5					
Early Bronze IB	J-4					

Figure 3.

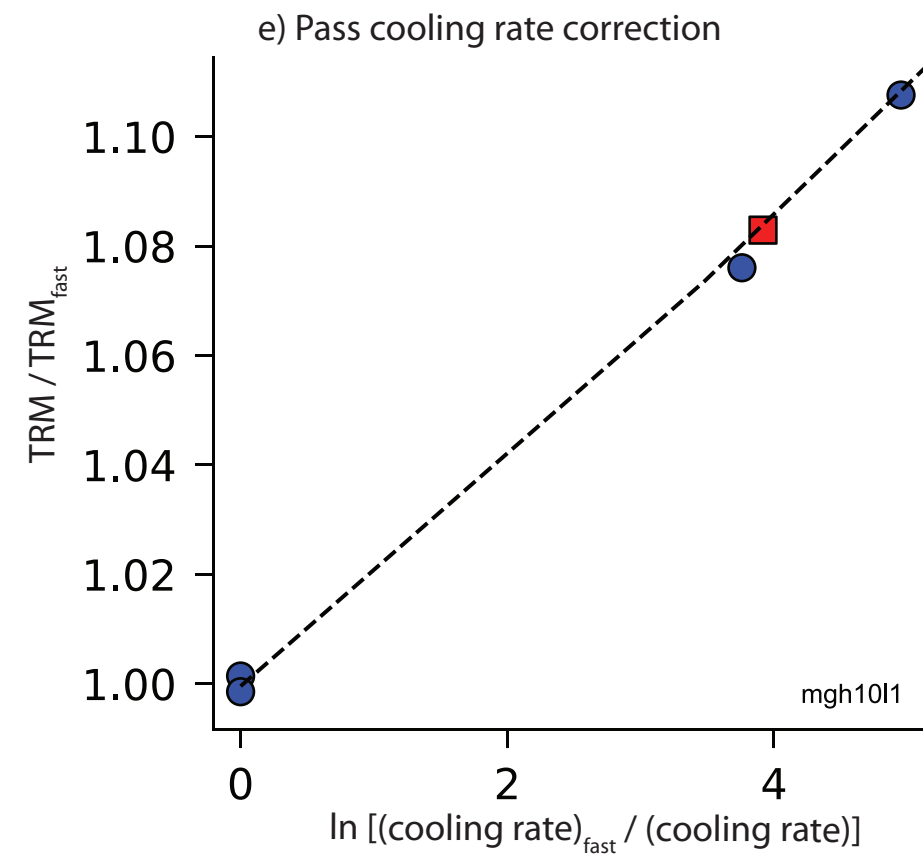
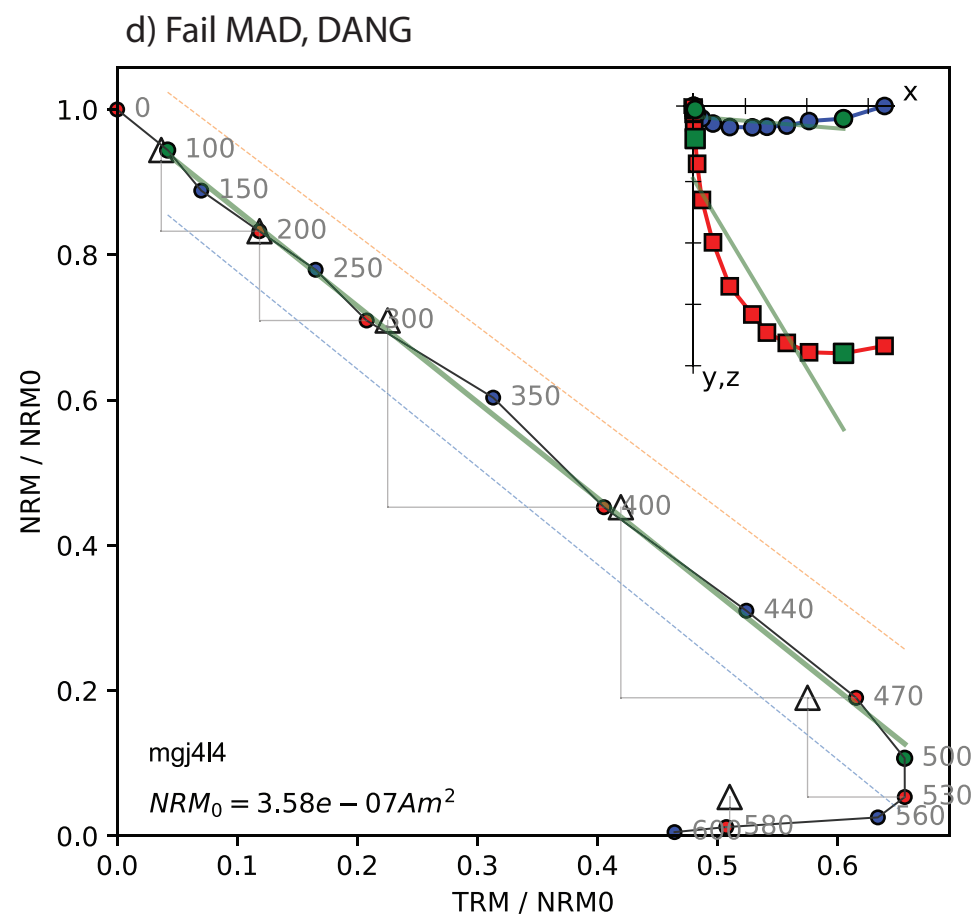
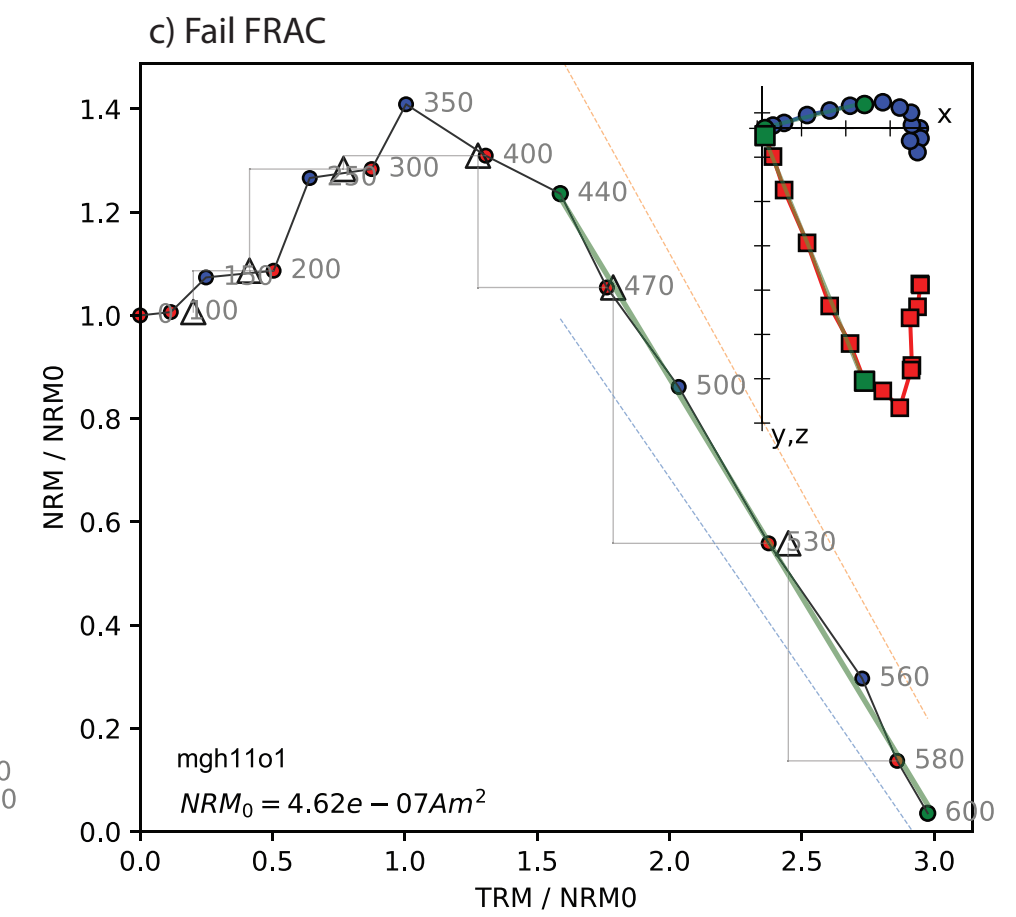
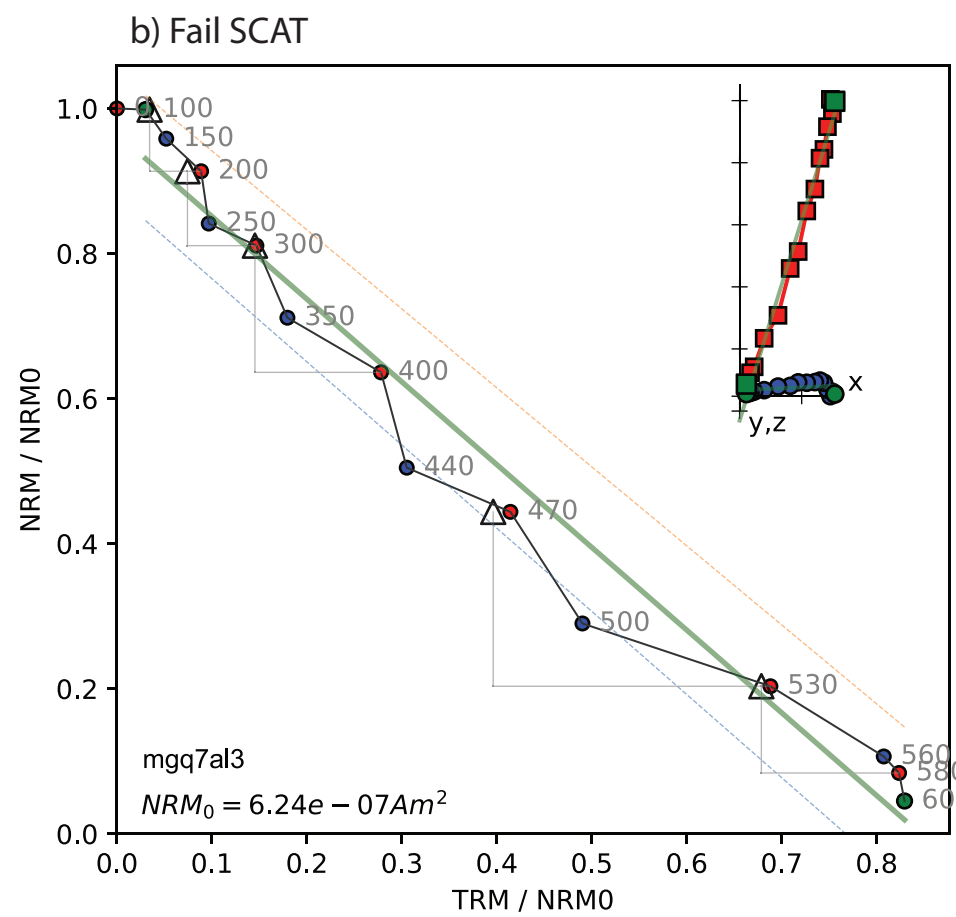
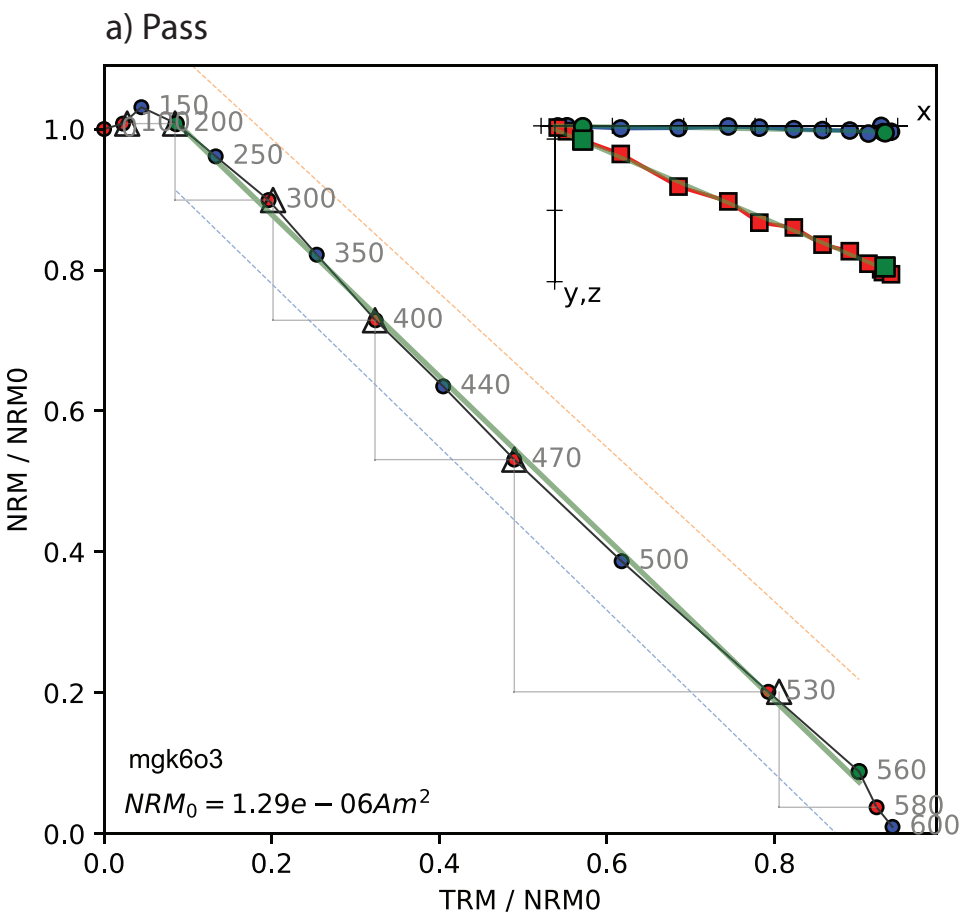
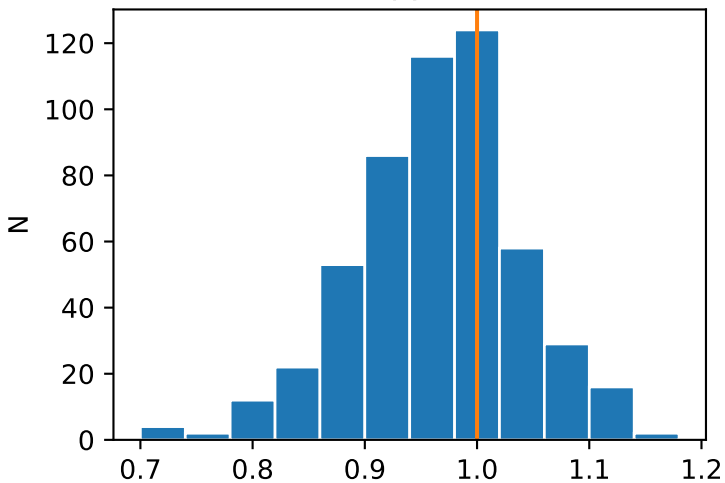
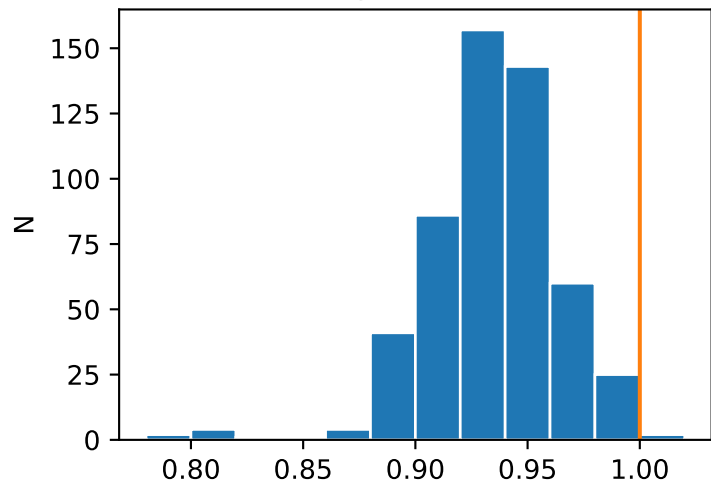


Figure 4.

a. Anisotropy correction



b. Cooling rate correction



c. Anisotropy + cooling rate corrections

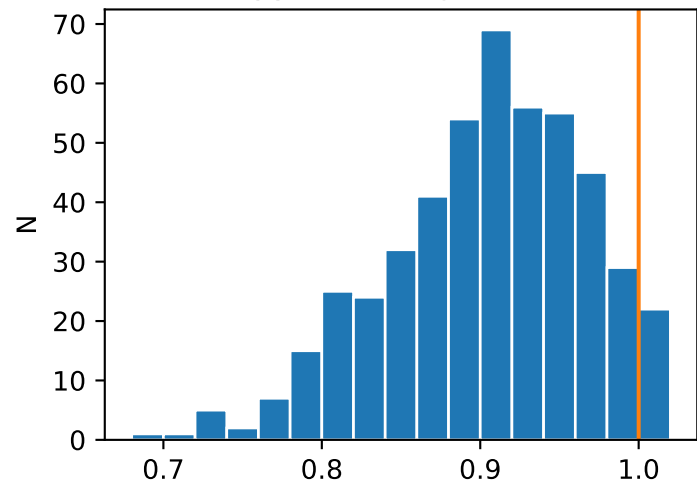


Figure 5.

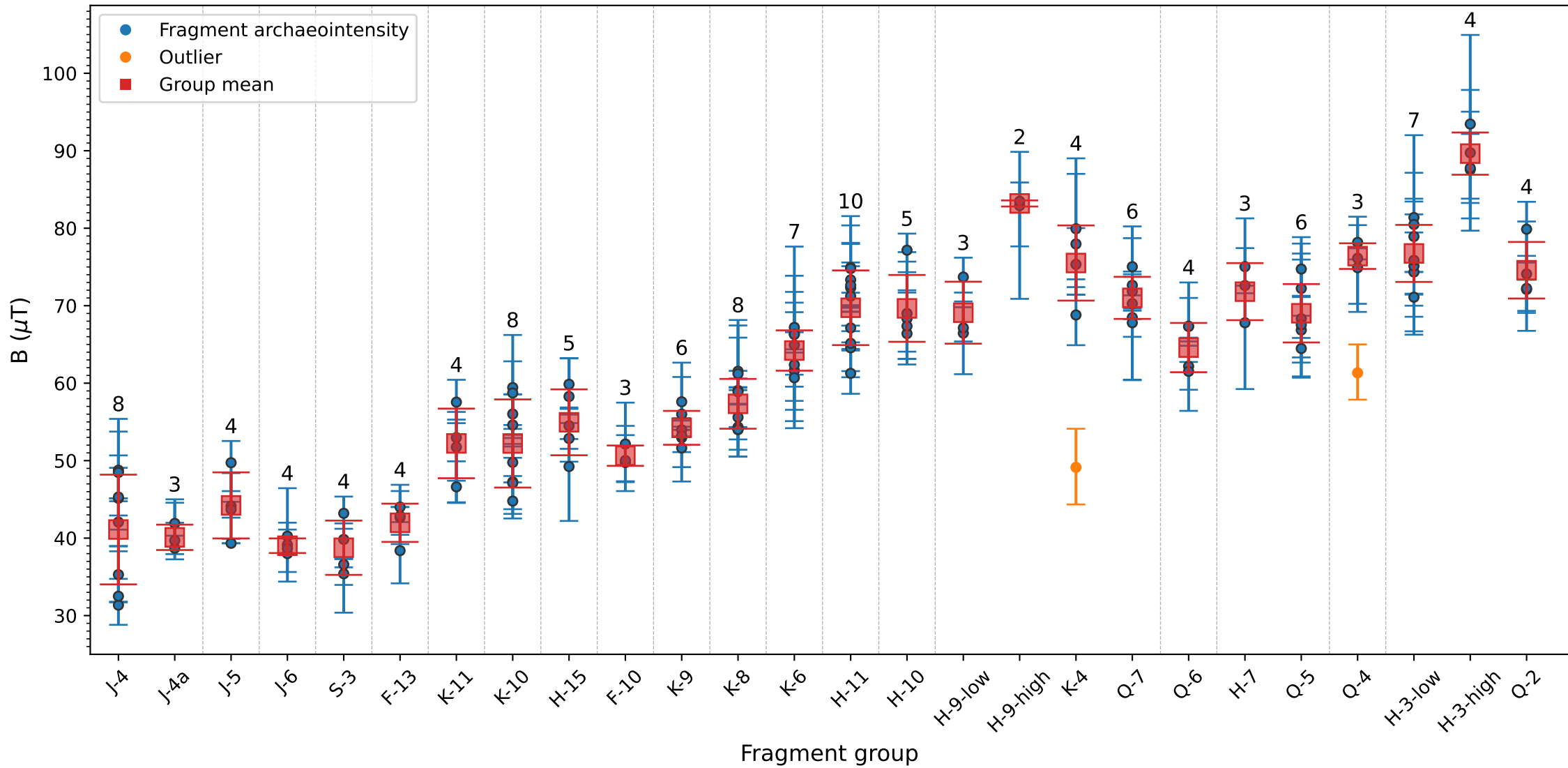


Figure 6.

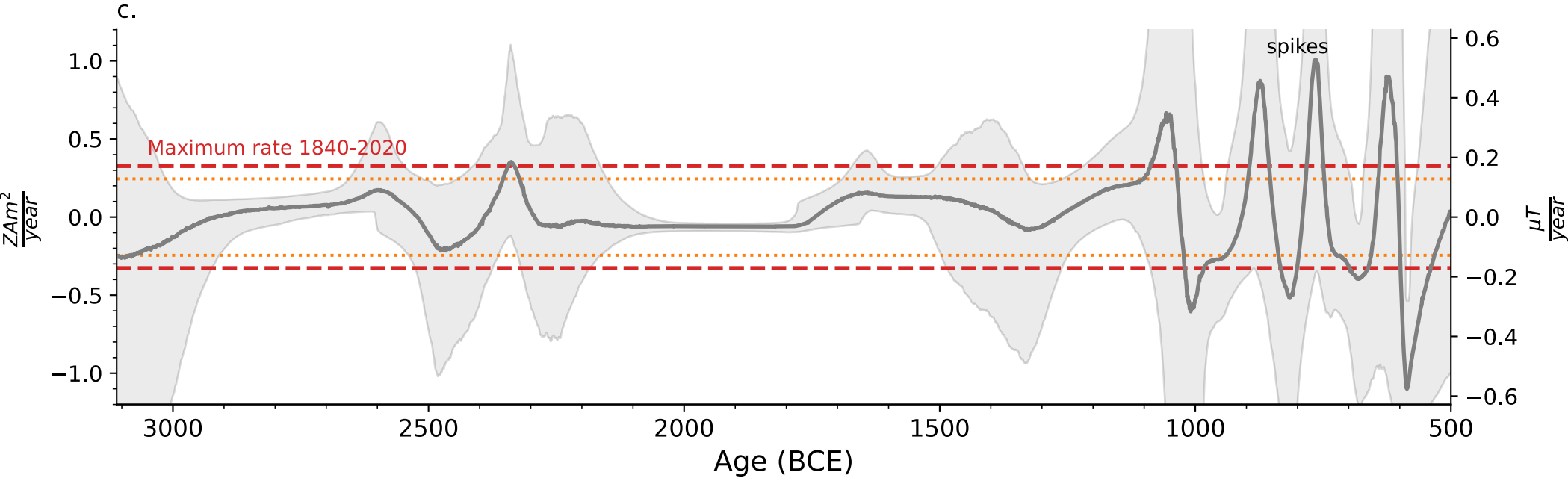
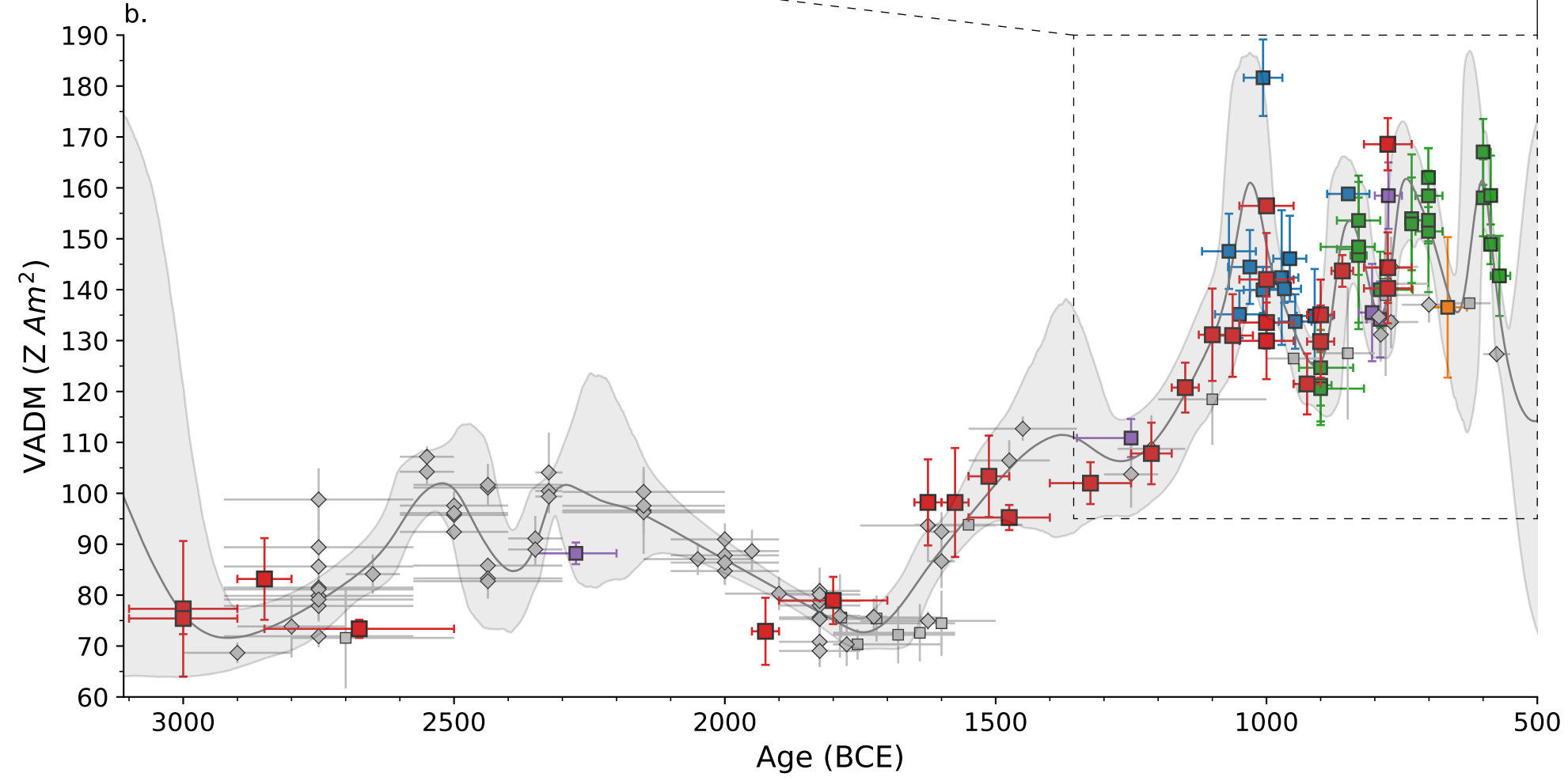
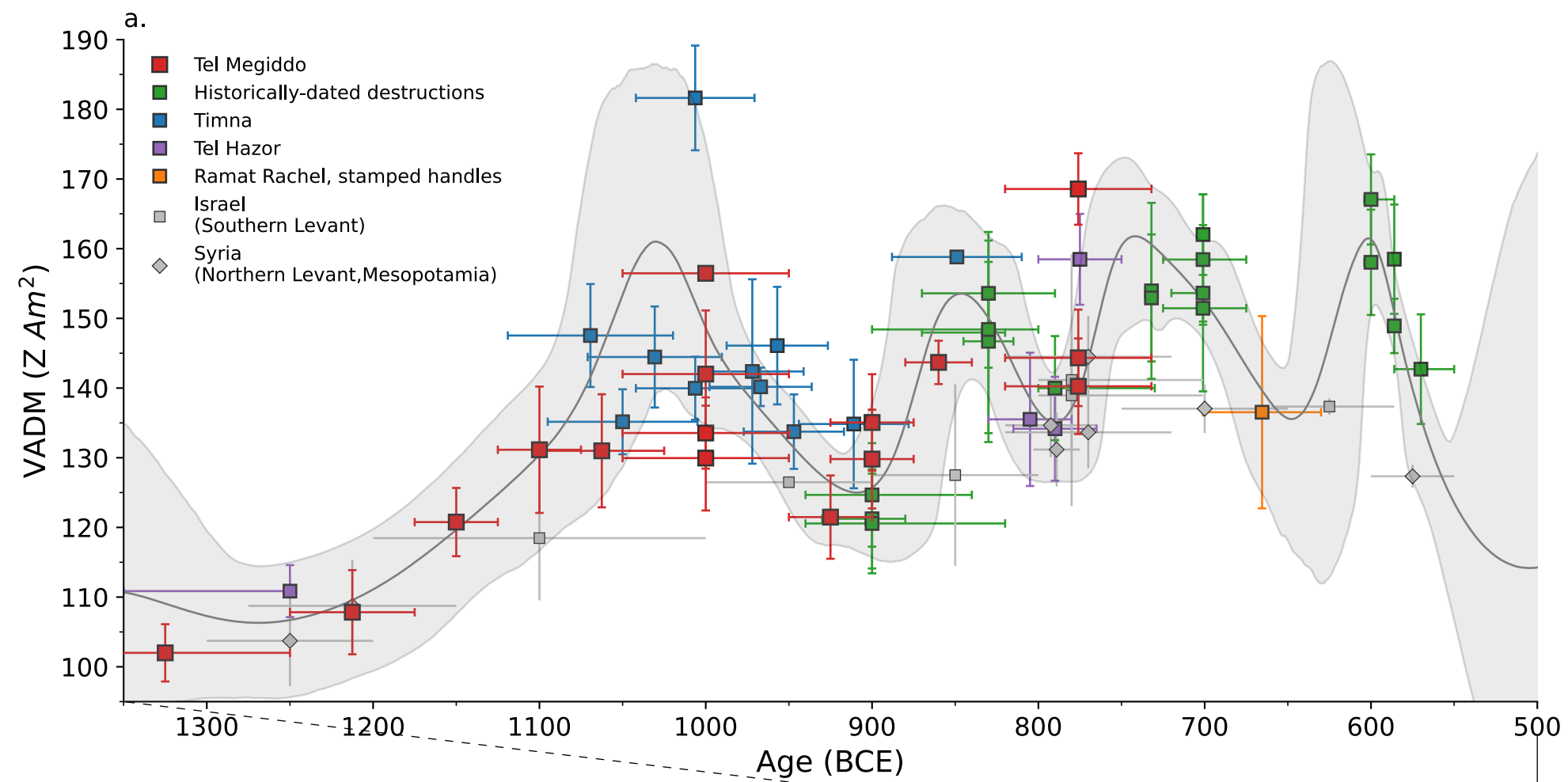
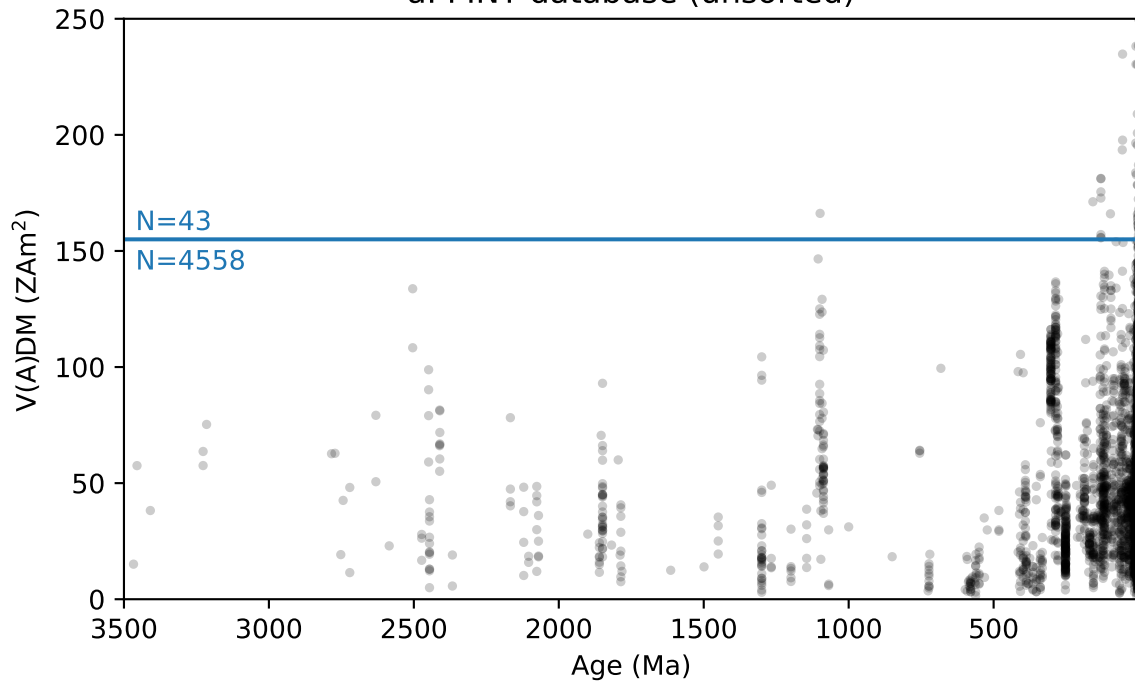


Figure 7.

a. PINT database (unsorted)



b. GEOMAGIA database (unsorted)

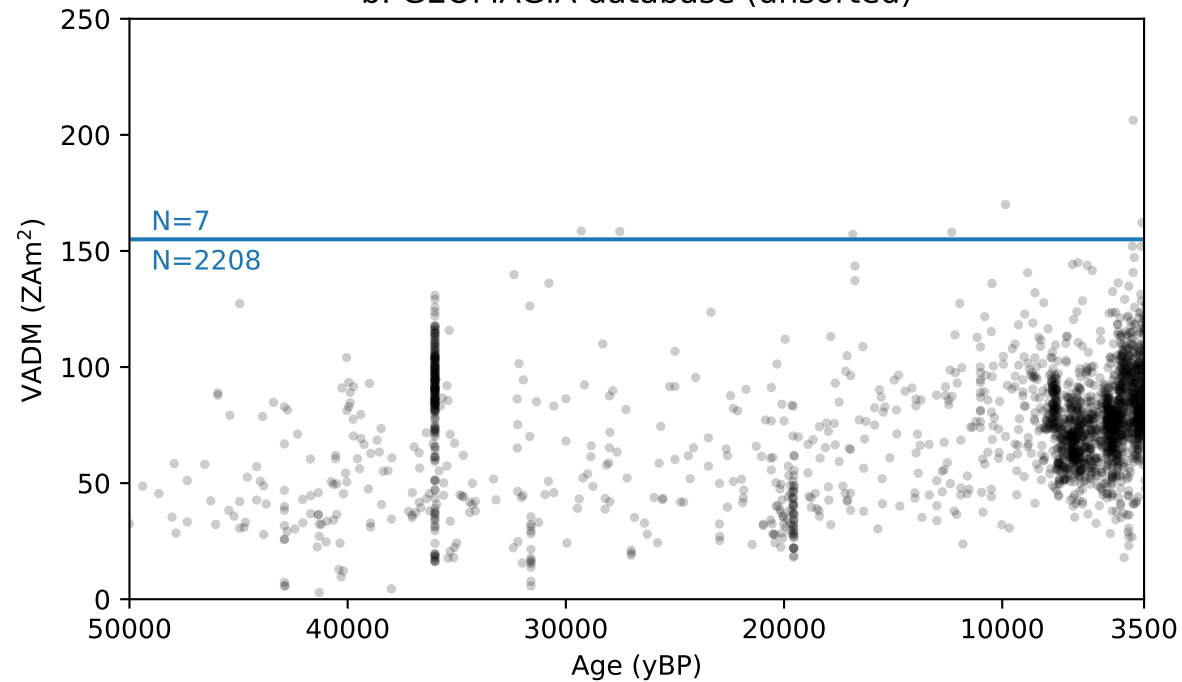
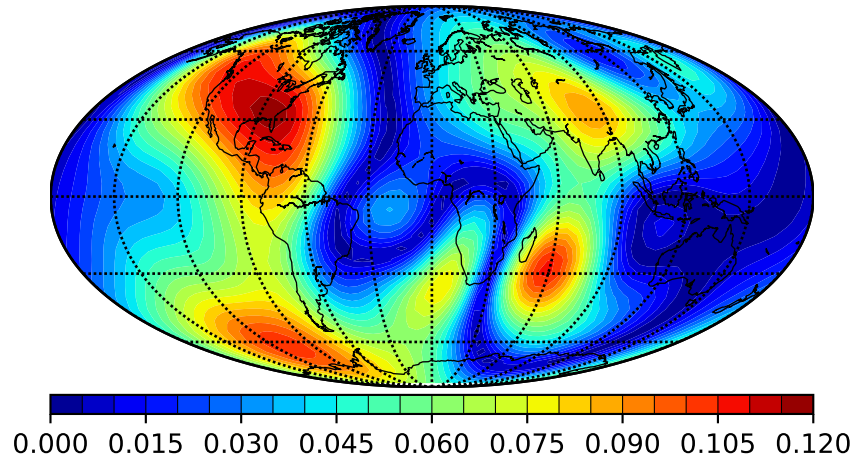
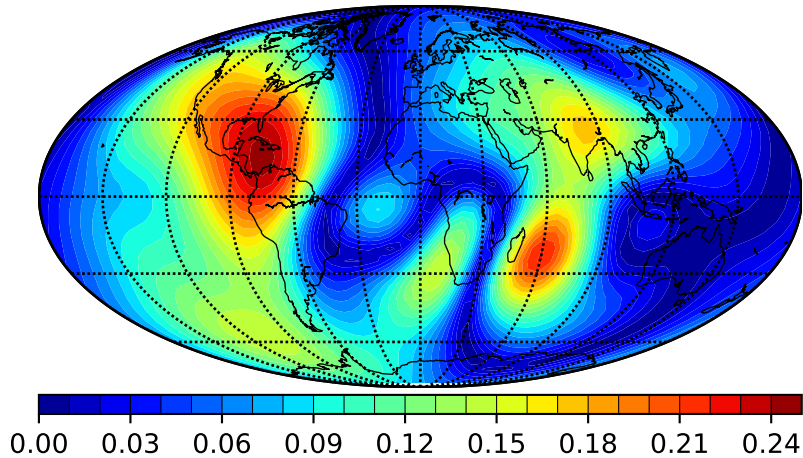


Figure 8.

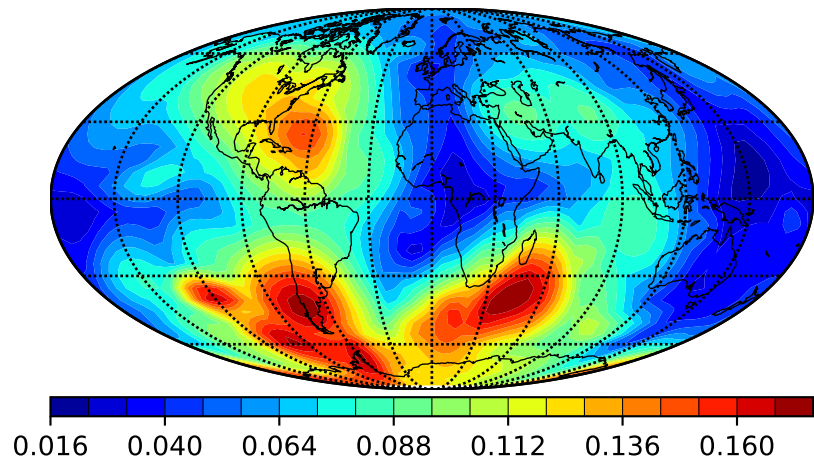
a. Maximum B rate of change ($\mu\text{T}/\text{year}$) 2020



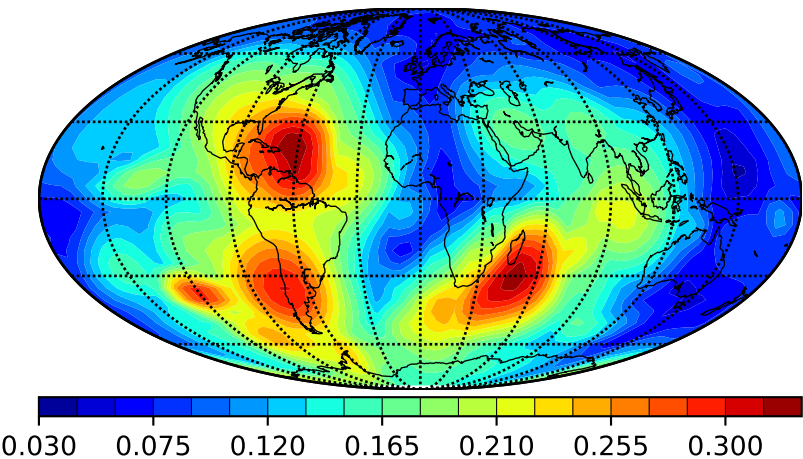
b. Maximum VADM rate of change (ZAm^2/year) 2020



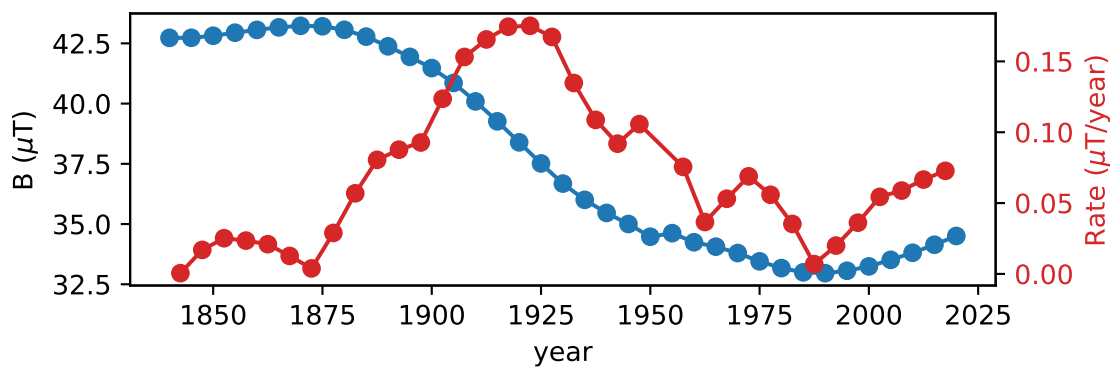
c. Maximum B rate of change ($\mu\text{T}/\text{year}$) 1840-2020



d. Maximum VADM rate of change (ZAm^2/year) 1840-2020



e.



f.

